Stony Brook University

Molecular Architecture of Amyloid Forming Peptides: Amyloid-β (1-42) and Prion Protein (118-135)

A Dissertation Presented

by

Mahiuddin Ahmed

To

The Graduate School

In Partial Fulfillment of the

Requirements

for the Degree of

Doctor of Philosophy

in

Biochemistry and Structural Biology

Stony Brook University

December 2009

Stony Brook University

The Graduate School

Mahiuddin Ahmed

We, the dissertation committee for the above candidate for the
Doctor of Philosophy degree, hereby recommend
acceptance of this dissertation.

Dr. Steven O. Smith - Dissertation Advisor
Professor, Biochemistry and Cell Biology

Dr. Daniel P. Raleigh - Chairperson of Defense
Professor, Chemistry

Dr. Erwin London
Professor, Biochemistry and Cell Biology

Dr. William E. Van Nostrand
Professor, Medicine

This dissertation is accepted by the Graduate School.

Lawrence Martin
Dean of the Graduate School

Abstract of the Dissertation

Structural Analysis and Inhibition of Amyloid Forming Peptides: Amyloid-β (1-42) and Prion Protein (118-135)

by

Mahiuddin Ahmed

Doctor of Philosophy

in

Biochemistry and Structural Biology

Stony Brook University

2009

Amyloid lesions found in several neurodegenerative and systemic diseases result from the alternative folding of cellular proteins into toxic aggregates. In particular, aggregation of the amyloid-β (Aβ) peptide has long been posited to be the primary causative agent for Alzheimer's disease pathology. In this study, high resolution 13C solid-state NMR spectroscopy was used to identify molecular contacts in fibrils and pre-fibrillar oligomers formed from the Aβ(1-42) peptide. The hydrophobic core of Aβ(1-42) fibrils consists of a β-hairpin motif with Phe19 opposite to Leu34 and Gln15 opposite to Gly37. The individual β-strands within a β-sheet were found to have a parallel and in-register orientation with a staggered, domain-swapped architecture. In soluble oligomers of Aβ(1-42) stabilized at 4°C, the peptide has a similar β-hairpin structure with the same Phe19 – Leu34 contact. However, the β-strands do not have a parallel and in-register

orientation and do not have a staggered domain-swapped architecture. When the Aβ42 stable oligomers are incubated at 37°C, they condense and elongate to form fibrils, as visualized using a combination of electron and atomic force microscopies. Stable oligomers of Aβ42 are significantly more toxic than fibrils when applied to primary mouse cortical neurons. The results indicate that pre-fibrillar oligomers of Aβ42, which have a defined β-hairpin structure, nucleate the formation of parallel and in-register domain swapped fibrils with diminished toxicity. A similar analysis was used to investigate the molecular packing arrangement of aggregates formed form the hydrophobic core of human prion protein, PrP (118-135). Amyloid fibrils formed from PrP (118-135) have a polymorphic structure where Met129 can pack against Gly127 and Gly131. Importantly, aggregation of both Amyloid-β (1-42) and prion protein PrP(118-135) can be inhibited by peptide inhibitors designed to block specific side-chain packing arrangements. Structural elucidation along with the development of structure-specific inhibitors may provide new therapeutic strategies towards ameliorating a wide range of amyloid-specific neurodegenerative and systemic pathologies.

For my parents and many teachers

Table of Contents

List of Figures

List of Tables

Acknowledgements

The author would like to gratefully acknowledge his parents, Dr. Mohamad Mizanur Rahman and Nargis Rahman for their unwavering love and support, and to rest of his family and friends.

He would also like to thank his previous research mentors, Prof. Robert Meyer at Brandies, Prof. Michael Squillacote at Auburn, Prof. Ned Porter at Duke, Prof. Carol Fierke at Duke and Michigan, and Prof. James Rothman at the Memorial Sloan-Kettering Cancer Center. Their immense guidance and support helped guide the interdisciplinary path taken in this work.

The author would like to acknowledge his advisor Prof. Steven Smith for the freedom to pursue the topics covered in this dissertation, for the engaging and insightful discussions, and for continued support throughout. It is under Prof. Smith's guidance that the author learned to become an independent scientist, and for this he will always be grateful. The author would also like to acknowledge his Chair Prof. Daniel Raleigh for immense professional guidance and counsel. The author is also grateful to Prof. Erwin London and Prof. William Van Nostrand for their guidance and support throughout the dissertation process.

The author would like to thank his many collaborators, without whom this work could not have been completed. He would like to particularly thank Dr. Iris Mastrangelo, Prof. Paul Hough, Dr. Martine Ziliox, Dr. Boris Itin, Prof. Michelle Poirier, Judianne Davis, Dr. Michael Hoos and to all of the members of Smith Lab, particularly Dr. Shivani Ahuja, Dr. Evan Crocker, and Dr. Takeshi Sato.

Lastly, the author would like to acknowledge the personal guidance from Dr. Sonia Sequeira and Joseph Michael Levry. Their work has inspired him to apply science in new ways and will continue to guide his future efforts.

Chapter 1

Introduction

Several neurodegenerative and systemic diseases are associated with the conversion of proteins into structures that differ from their native states. The pathological states that rsult are referred to as protein misfolding diseases, which include Alzheimer's disease, transmissible spongiform ecephalopathies (prion diseases), Parkinson's disease, Huntington's disease, and Type II Diabetes. The majority of these misfolding diseases are associated with the conversion of a soluble cellular protein or peptide fragment into highly structured fibrillar aggregates, known as amyloid fibrils (1). The observation of these fibrillar deposits in diseased tissue has led to intensive research on the mechanisms of amyloid formation and the pathways involved in toxicity. While there continues to be much debate as to whether these diseases are caused by the gain-of-function of toxic amyloid assemblies or the loss-of-function of normal cellular protein precursors, a growing body of literature has shown that amyloid fibrils and particularly soluble pre-fibrillar oligomers can cause pathology in both tissue culture and animal models (2). Investigation into the high-resolution structures of amyloid fibrils and pre-fibrillar oligomers has become of great interest in an effort to design novel diagnostic and therapeutic agents.

Table 1.1: Neurodegenerative and systemic diseases associated with both amyloid fibrils and pre-fibrillar oligomers (3).

Protein or peptide	Disease	Affected Tissue
Aβ peptide	Alzheimer's disease	Brain
Prion protein	transmissible spongiform encephalopathies: Creutzfeldt-Jakob disease, Kuru, fatal familial insomnia, Gerstmann-Straussler-Scheinker disease	Brain
α-synuclein	Parkinson's disease	Brain
Huntingtin	Huntington's disease	Brain
Stefin (cystatin) B	Myoclonus epilepsy type 1	Brain
Islet amyloid polypeptide (amylin)	Type II diabetes mellitus	Pancreas
Human lysozyme	Familial or hereditary amyloidosis	Liver, kidney
Transthyretin	Familial amyloid polyneuropathy	Peripheral nerve
Immunoglobulin light chain	Primary amyloidosis	Kidney, lung, heart
Apolipoprotein A1	Familial or hereditary amyloidosis	Heart
Desmin	Desmin-related cardiac amyloidosis	Heart

1.1 Structure of amyloid fibrils

Amyloid fibrils are typically 7-13 nm wide and often contain multiple protofilaments (striations seen in electron microscopy images) that twist along the main fibril axis (1). They exhibit cross-β X-ray diffraction patterns, have β-sheet rich circular dichroism (CD) and Fourier transform infrared (FTIR) spectra, and have core structures that are resistant to hydrogen exchange (4). Diagnostic markers of amyloid include the use of the dyes Congo red and Thioflavin T or its analogues. Most amyloid fibrils display green

birefringence under polarized light when bound to Congo red and alter the fluorescent properties of Thioflavin T and its analogues upon binding (5).

The earliest structural information on amyloid fibrils came from X-ray diffraction studies showing that fibrils have a cross-β structure (6). A cross-β structure refers to β-strands that orient perpendicular to the long axis of fibrils, allowing the β-strands to hydrogen bond along the fibril length (see Figure 1.1). Side-chain packing interactions (perpendicular to hydrogen bonding direction) determine the number of cross-β units along the fibril width. A typical cross-β X-ray diffraction pattern has perpendicular reflections at ~4.7 Å along the meriodonal (long) direction and ~10 Å along the equatorial dimension (see Figure 1.1)(7). The 4.7 Å distance represents the main-chain spacing between β-strands along the fibril length, whereas the 10 Å distance represents the side-chain spacing between adjacent β-strands along the fibril width. This is in contrast to parallel-β structures such as β-keratin and silk, where β-strands orient parallel to the long fibrillar axis (5).

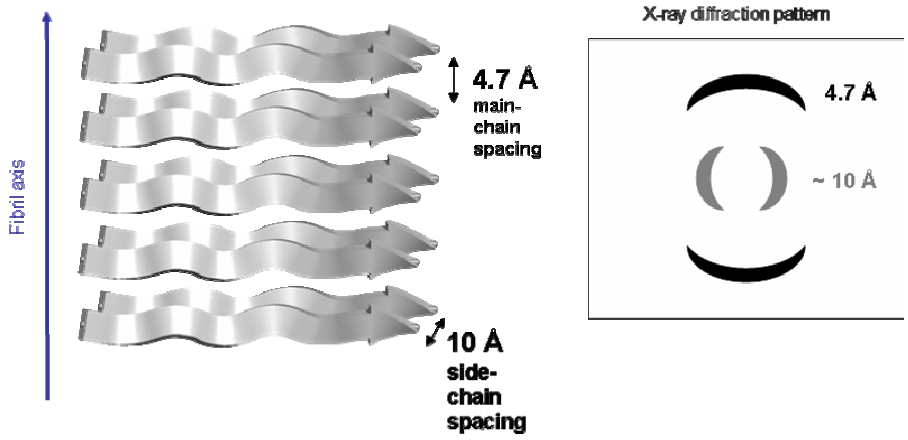

Figure 1.1: Schematic of a cross-β structure and typical X-ray diffraction pattern of an amyloid fibril.

Investigation into the molecular details of the cross-β structure of amyloid fibrils was limited by fibrils not being crystalline enough for high-resolution X-ray crystallography analysis and not being soluble enough for solution NMR studies. Major advances came from the application of solid-state NMR to understanding fibril architecture. The first solid-state NMR studies were done on amyloid-β(39-42), a small 9-residue carboxy-terminal fragment of the amyloid-β (Aβ) peptide associated with Alzheimer's disease (8, 9). The analysis showed that the cross-β structure of amyloid-β(39-42) is composed of anti-parallel β-sheets. Tycko and co-workers went onto investigate longer fragments of the amyloid-β peptide and found that Aβ(10-35) and Aβ(1-40) contained parallel and in-register β-sheets, where each residue on one β-strand lines up with the same residue on the next adjacent β-strand along the fibril length. Full models of Aβ(1-40) fibrils based on solid-state NMR and computational modeling revealed that each molecule contributes a pair of β-strands in a hairpin configuration,

with two to three hairpin units per 4.7 Å fibril cross-section (10, 11). A number of solid-state NMR models have since been developed for other amyloid-forming proteins and peptides, and the prevailing architecture has been that of parallel β-sheets (10).

A next major advance in gathering high-resolution structural data of amyloid fibrils came from the ability to perform high-resolution X-ray crystallography on micro-crystals formed from short amyloid-forming peptides. The first such analysis came from Eisenberg and co-workers, who formed three-dimensional crystal from the GNNQQY sequence form the yeast prion Sup35p (12). The crystals contained pairs of parallel and in-register β-sheets, with each peptide contributing a single β-strand. The paired β-sheets tightly interacted with one another through side-chains interactions at Asn2, Gln4, and Asn6. The side-chain interaction was so tight that it excluded water, and led to using the term "steric zipper" to describe this side-chain packing architecture. Further studies of other short amyloid forming segments, including fragments of Alzheimer's amyloid-β and tau proteins, prion protein, insulin, islet amyloid polypeptide (IAPP), lysozyme, myoglobin, alpha-synuclein and β2-microglobulin, were all found to form parallel β-sheet structure of varied steric zipper interactions (13).

The solid-state NMR and X-ray crystallographic data suggested that the wide range of amyloid-forming proteins may have very similar core structures. Subtle variations in the fine molecular architecture, such as specific side-chain packing, may lead to the wide variety of clinical outcomes involved in the various protein misfolding diseases.

1.2 Formation of amyloid intermediates

Amyloid fibril formation typically exhibits nucleation-polymerization kinetics where an initial lag phase is followed by a rapid acceleration to fibril formation (14). Along this path, the amyloid forming protein or peptide can adopt a number of conformations. In a cellular environment, the newly generated protein or peptide can populate a variety of conformations before forming fibrils or fibril-like structures (see Figure 1.2). These conformations can form depending on cellular regulation as well as genetic and environmental factors. In a more simplified microscopic framework, amyloid conformations typically exist is three morphologically distinct states: oligomers, protofibril, and mature fibrils. *Oligomers* refer to the metastable multimers produced during the kinetic lag phase and are often imaged as spherically aggregates. *Protofibrils* refer to non-spherical elongated structures that microscopically appear "rod-like" or "worm-like" (4). Mature *fibrils*, in addition to the biophysical characteristics mentioned in the preceding section, appear as relatively straight, unbranched filaments with periodic twisting along the main fibril axis. Pre-fibrillar oligomers have been implicated to be the primary pathological agent in several protein misfolding diseases including the ones listed in Table 1.1.

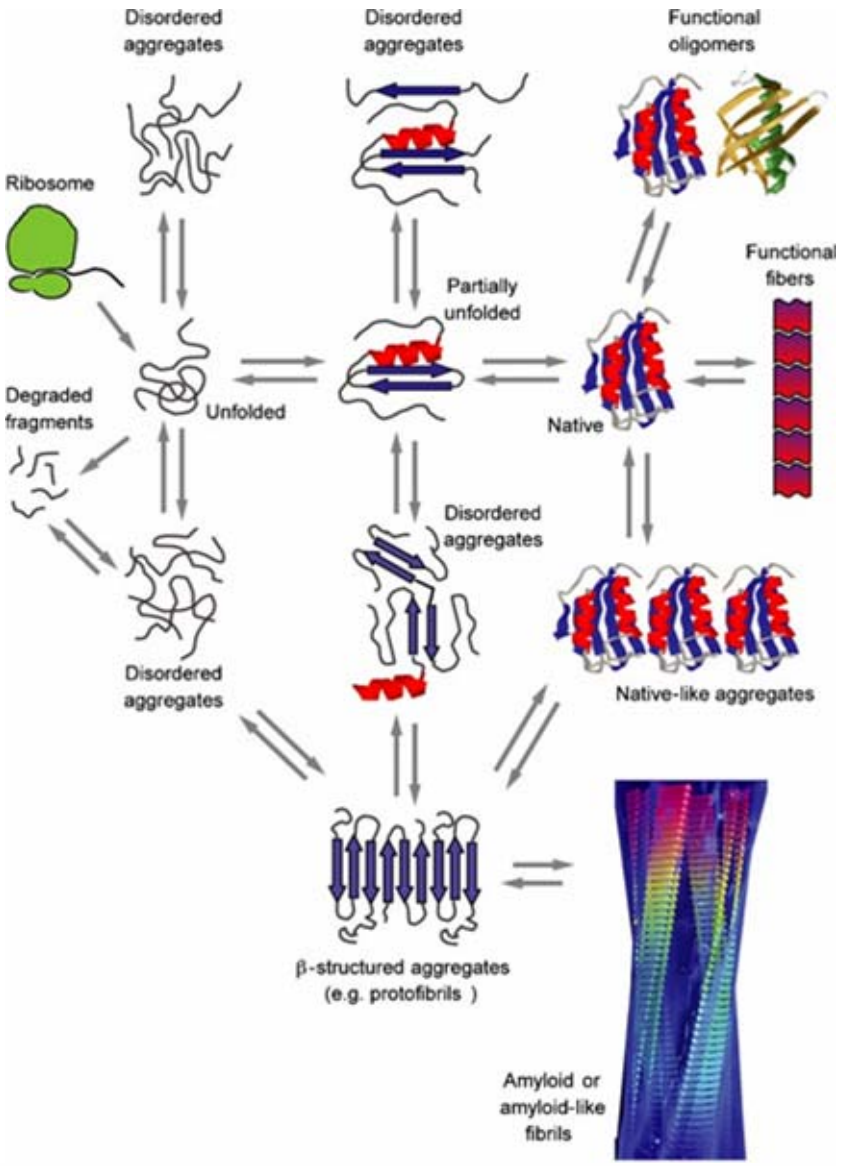

Figure 1.2: Schematic of the various intermediates along the pathway of forming amyloid fibrils, from *Chiti and Dobson* (1).

1.3 Amyloid formation in Alzheimer's and prion diseases.

The focus of this study has been to investigate the structures of the two amyloid forming peptides: Amyloid-β (Aβ) and prion protein (PrP), which have been implicated to be the primary causative agents in the pathogenesis of Alzheimer's disease and transmissible spongiform encephalopathies (prion diseases), respectively. Despite the drastic differences in disease phenotypes, Aβ and PrP have remarkable similarities in structure, localization, processing, and toxic function, and both undergo structural transitions that lead to a toxic gain-of-function characteristic of causing neurodegeneration (15, #5143). In addition, recent evidence has provided a direct link between Aβ and PrP, showing that non-pathogenic cellular PrP directly inhibits the generation of toxic Aβ peptides by blocking the action of β-secretase, a key enzyme in proteolytic processing and generation of Aβ (16).

The precursor of Aβ production, amyloid precursor protein (APP), and cellular PrP both localize to the plasma membraneof cells in the central nervous system and other tissues. Membrane interactions, particularly in cholesterol and sphingolipid-rich lipid rafts, have been implicated as important for the pathological conversion of cellular PrP, and for the proteolytic production, degradation, and aggregation of Aβ (17). The transmembrane domain of APP (including the carboxy-terminal half of Aβ) as well as the putative transmembrane domain of PrP (residues 110-134) contain three highly conserved GxxxG motifs. The GxxxG motif has been well characterized for its ability to mediate transmembrane helix interactions (18, 19). In a screening assay to determine homo-oligomerization in membranes, >80% of sequences that interact out of 1×10^7 sequences were found to contain the GxxxG motif (20). When glycines are separated by three residues in a transmembrane helix, they line up on the same face, and given the small size

of glycine residues relative to other amino acids, the pair of glycines can form a molecular notch to facilitate inter-helical packing (21). The presence of the three consecutive GxxxG motifs and the functional consequences involved in the membrane interactions in both Aβ and PrP highlight the importance of investigating the transmembrane regions to better understanding the pathological conversions of α-helical transmembrane domains to β-sheet rich amyloid aggregates.

In addition to the three consecutive GxxxG motifs in Aβ and PrP, a critical methionine residue in the third GxxxG motif is common to both (Met35 in Aβ and Met129 in PrP), forming a GxMxG sequence. Met35 in Aβ is involved in modulating neurotoxicity by a playing a role in Aβ redox chemistry (22, 23). Met129 in PrP is the site of important polymorphism that modulates disease susceptibility in human prion diseases and is a risk factor for early onset Alzheimer's disease (24, 25). The PrP gene (PRNP) can encode methionine or valine at position 129. Homozygotes of Met129 or Val129 are more susceptible to the prion disease Creutzfeldt-Jakob disease (CJD), and only homozygotes of Met129 have ever developed variant CJD, known as bovine spongiform encephalopathy (24, 25). It is likely that these critical methionines may also have a role in the structure and toxicity of amyloid conformations of Aβ and PrP.

Table 1.2: GxxxG motifs in amyloid forming sequences. Aβ(1-42) and PrP(118-135) contain three consecutive GxxxG motifs. All three sequences contain a GxMxG motif.

PROTEIN OR PEPTIDE	**SEQUENCE**
Aβ(1-42)	DAEFRHDSGYEVHHQKLVFFAED - VGSNKGAIIGLMVGGVVIATVIVITLVMLK
PrP(118-135)	AGAVVGGLGGYMLGSAMS
Glycophorin A (70-98)	EPEITLIIFGVMAGVIGTILLISYGIRRL

To investigate the structural features involved in forming amyloid fibrils from proteins that contain transmembrane GxxxG motifs, Smith and co-workers tested the ability of the transmembrane domain of glycophorin A, cell-surface glycoprotein that homo-dimerizes due to a conserved GxxxG motif and a central methionine residue (GxMxG), to form amyloid fibrils (see Table 1.2)(26). Glycophorin A had never previously never been shown to form amyloid structures. They found that the truncated transmembrane domain of glycophorin A which contained the GxMxG sequence formed amyloid fibrils in aqueous environments with a parallel and in-register orientation. Using solid-state NMR, they showed that the small size of glycine residues in extended β-conformations facilitated the side-chain packing of bulky hydrophobic side-chains such as methionine on adjacent β-strands along the fibril width (see Figure 1.3). The proposed side-chain packing, termed "dovetail" packing, closely resembles the "steric zipper" models later developed by Eisenberg and co-workers.

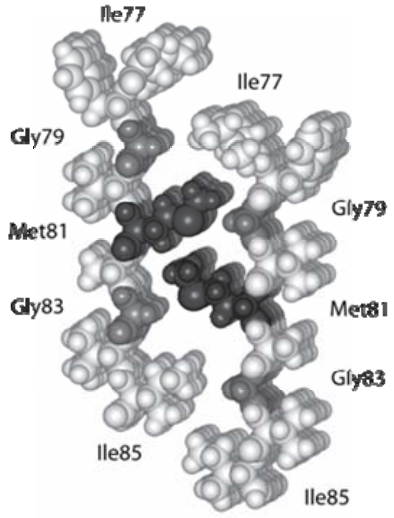

Figure 1.3: Dovetail packing within GpA70-86 fibrils, from *Liu et al.* (26). Cross sectional view of parallel and in-register amyloid fibrils where molecular notches formed by Gly79 and Gly83 facilitate the side-chain packing of Met81.

The results from the glycophorin study suggest that glycine may not only play an important role in inter-helical packing of transmembrane domains, but also provide stabilizing notches to promote the formation of amyloid fibrils in aqueous environment. Due to the sequence similarities with Aβ and PrP, the objective of this study was to investigate the molecular architecture of the full length Aβ(1-42) peptide and the fragment of the transmembrane domain of prion protein, PrP(118-135), with particular interest in the role of conserved glycine and methionine residues. The structural insights would then be used to design novel peptide inhibitors to block side-chain packing interactions.

Chapter 2

Methods

2.1 Amyloid Sample Preparation

Purified ^{13}C-labeled peptides of Aβ and PrP(118-135) were purchased from W.M. Keck Facility (Yale University, New Haven, CT). Fibril and soluble oligomer samples were prepared by first dissolving purified peptides in 1,1,1,3,3,3-hexafluoro-2-propanol (HFIP) to dissolve any pre-formed aggregates. Dissolved HFIP/peptide solutions were then flash frozen in liquid nitrogen and lyophilized under low pressure (<10 mtorr) and low temperature (-80 C) to completely remove HFIP solvent.

For oligomer studies, peptides were initially dissolved in a small volumes of dilute NaOH, and then brought up in either low salt buffer (10 mM phosphate buffer, 10 mM NaCl) and titrated to pH 7.4 with dilute acid (200 μM final peptide concentration). Samples were immediately filtered with a 0.2 μm cellulose acetate syringe filter and kept at 4°C for up to 6 h and analyzed by electron microscopy, atomic force microscopy (AFM), and immunoblot analysis or flash frozen in liquid nitrogen and lyophilized for solid-state NMR studies.

For fibril studies, peptides were initially dissolved in a small volumes of dilute NaOH, and then brought up in either physiological salt buffer (10 mM phosphate buffer, 100 mM NaCl) and titrated to pH 7.4 with dilute acid (200 μM final peptide concentration). Samples were immediately filtered with a 0.2 μm cellulose acetate syringe filter and then incubated at 37°C with gentle agitation for 12 days for Aβ peptides and 4 days for PrP(118-135) peptides. Samples were analyzed by EM and AFM. For NMR studies, samples were pelleted, rinsed with Millipore water and lyophilized for solid-state NMR studies. It has been established that lyophilization of Aβ oligomers and fibrils does not appreciably perturb the structure or hydrated oligomers and fibrils (10, 27).

2.2 Transmission electron microscopy

Amyloid samples were diluted and deposited onto carbon-coated copper mesh grids for transmission EM imaging. Carbon-coated grids resulted in higher resolution and less staining artifacts than formvar coated grids. Sample grids were negatively stained with 2% (w/v) uranyl acetate. The excess stain was removed, and the sample grids were allowed to air dry. The samples were imaged with a FEI Tecnai 12 BioTwin 85 kV transmission electron microscope at the Central Microscopy Imaging Center (Stony Brook University, Stony Brook, NY). Digital images were taken with an Advanced Microscopy Techniques camera.

Figure 2.1 shows an EM image of Aβ42 peptides incubated at 37 °C for 24 h. At this time point, round oligomers, elongated protofibrils and newly formed fibrils can be observed.

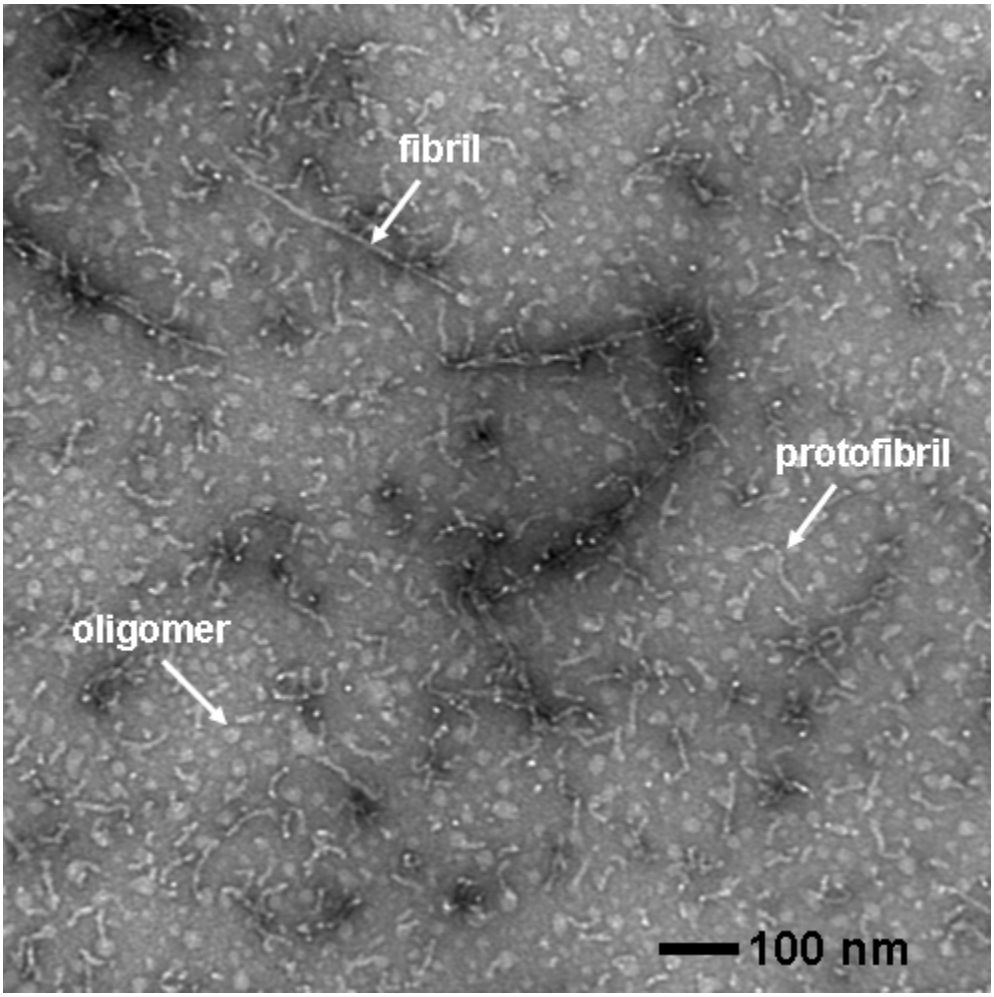

Figure 2.1: EM image of Aβ42 peptides incubated at 24h at 37 °C.

2.3 Single-touch atomic force microscopy

Atomic force microscopy (AFM) is a scanning probe microscopy developed to measure the topology of a three dimensional surface at ultra-high resolution. There are two conventional methods for AFM: tapping mode (28-30) and contact mode (see Figure 2.2)(31, 32). In contact mode, the scanning tip is in constant contact with the surface. This limits its use for imaging biological samples due to the transverse force of the tip, which can sweep particles out of the imaged fields. Tapping mode, on the other hand, where the scanning tip is in constant oscillation with the sample surface, has had some success in imaging isolated proteins ad DNA fragment (33). Tapping mode, however, can distort biological sample because of the high compressive force applied during the tip approach, the multiple contacts with the sample at each approach pixel, and greater uncertainty of the height measurement.

A new method of AFM designed to overcome these limitations was used to characterize the fine structure of amyloid oligomers and fibrils in this study. The technique, designated as single-touch AFM (LifeAFM, Port Jefferson, NY), uses a computer controlled approach over every pixel, termed LifeScan. When contact is made with the sample surface at a given pixel, the tip (which has an attached magnetic particle) is pulled off of the sample by applying a magnetic field directly above the sample apparatus. This is done at every single approach such that there is one contact per pixel. This eliminates the transverse force associated to contact mode AFM and the high compressive forces and imprecision of tapping mode AFM, allowing for ultra-high resolution of biological samples.

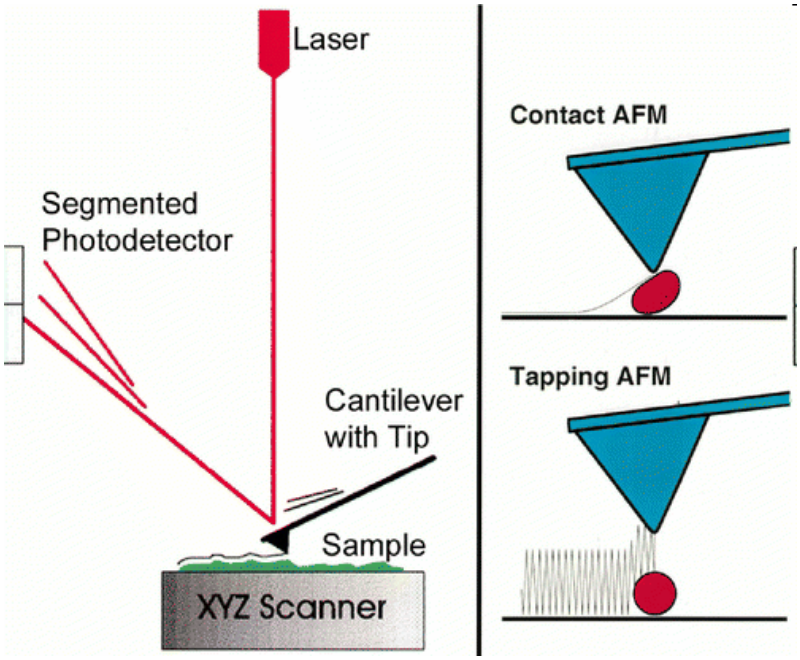

Figure 2.2: Schematic of standard tapping and contact mode AFM, from *Hansma et al.* (33). Lateral and vertical sample movement is controlled by a piezo-electric crystal. Height measurements are detected from the deflection of a laser beam from the scanning cantilever/tip onto a diode array detector.

AFM was carried out using the LifeScan controller developed by LifeAFM (Port Jefferson, NY) interfaced with a Digital Instruments (Santa Barbara, CA) MultiMode microscope fitted with an E scanner. The computer control of the cantilever position and angle during approach allows for detection of the sample height with minimum cantilever deflection, allowing for a minimum compressive force (30-100 picoNewtons/nm) applied to the sample. AFM samples were prepared by adsorbing 20 µL of sample mixture to freshly cleaved ruby mica or highly oriented pyrolytic graphite, HOPG (S & J Trading, Glen Oaks, NY). Samples were imaged under hydrated conditions using super-sharp

silicon probes (SSS-Cont, Nanosensors, Neuchatel, Switzerland) that were modified for magnetic retraction by attaching samarium cobalt particles. The effective diameters of the super-sharp silicon probes are estimated to be 4 ± 1 nm at a height of 2 nm. Data analysis and graphics was performed using Interactive Display Language 5.0 (Research Systems Inc., Boulder, CO). In the Z scale bars, numbers in each color square indicate the Z-value at the middle of the range for that color.

Various amyloid forming peptides have different affinities for the surfaces used in AFM imaging. The two surfaces most commonly used, ruby mica and HOPG, also differ in their surface properties. Ruby mica is the preferred substrate and is more atomically flat and has a negatively charged surface. HOPG is less flat, with periodic steps along the surface, and is more hydrophobic. Amyloid oligomer samples have little difficulty adhering to mica surfaces, but when they polymerize into fibrils, they do not stick to negatively charged mica surfaces under the hydrated conditions necessary for single-touch AFM (hydration dampens the compressive force of the scanning tip). This is true for Aβ40, Aβ42 and PrP(118-135).

This technical difficulty can be overcome by two methods: using HOPG, or acidifying the sample immediately before depositing onto mica. Figure 2.3 illustrates the first strategy. Aβ40 fibrils (incubated for 5 d at 37°C) were deposited onto mica and HOPG. The mica substrate only showed the presence of oligomers, whereas HOPG displayed the fibrils and background oligomers. In Figure 2.4, the second strategy is illustrated. Here Aβ42 fibrils (incubated for 6 h or 7 d at 37°C) were titrated to pH 4 with dilute acid and immediately deposited onto mica. Protofibrils and fibrils can be seen under these conditions.

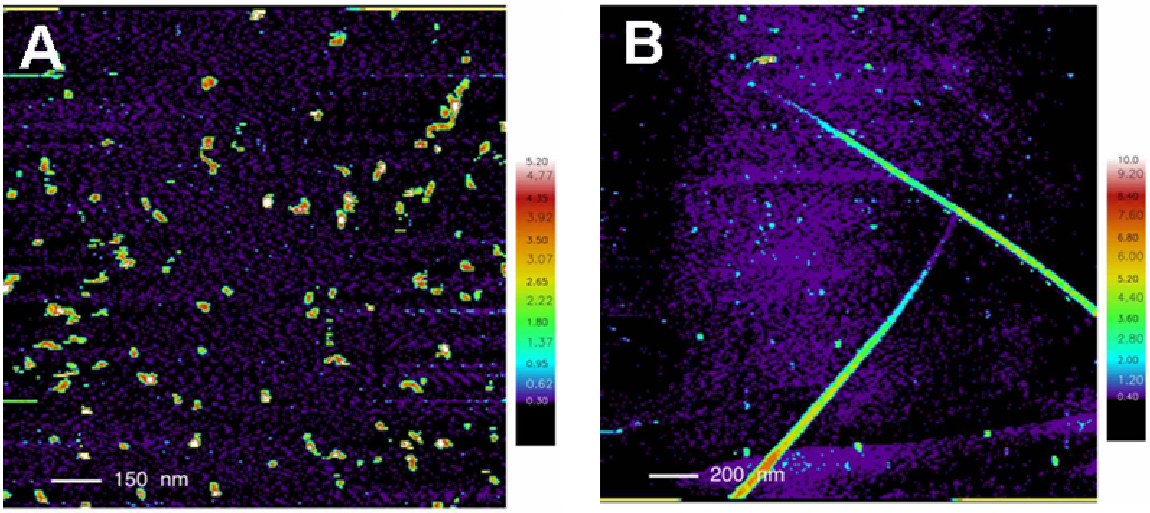

Figure 2.3: Aβ40 fibrils deposited onto mica (A) or highly oriented pyrolytic graphite (B).

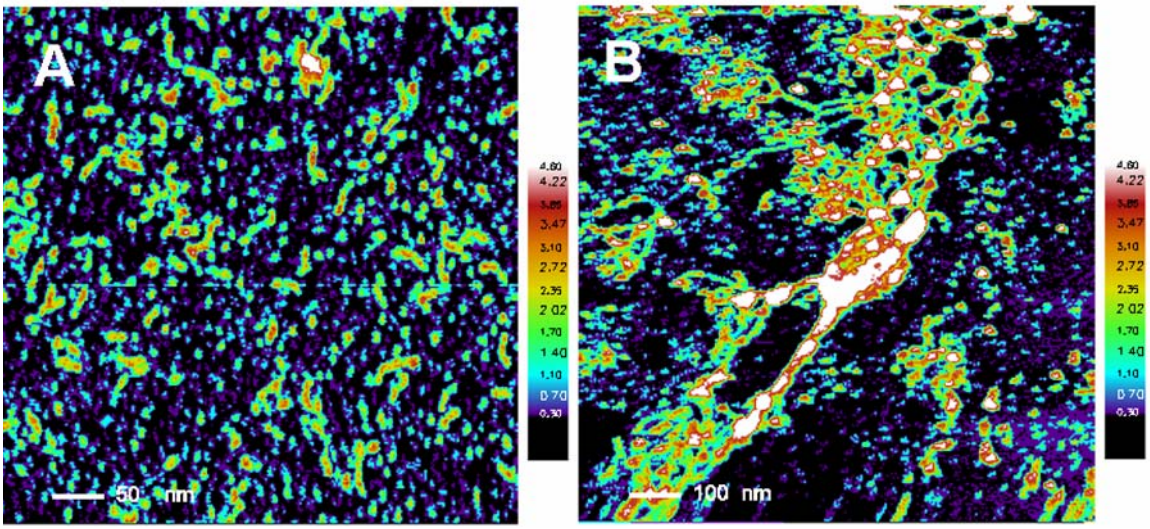

Figure 2.4: Aβ42 protofibrils (A) and fibrils (B) deposited onto ruby mica at pH 4.

Although fibrils made from wild-type Aβ40 and Aβ42 peptides have difficulty adhering to mica, a mutant of Aβ40 carrying both the Dutch and Iowa familial mutations E22Q and D23N adhere to mica at pH 7.4 (see Figure 2.4). This double mutation causes an enhanced fibrillogenesis kinetics with fibrils being well-formed in 6 h of incubation at 37°C.

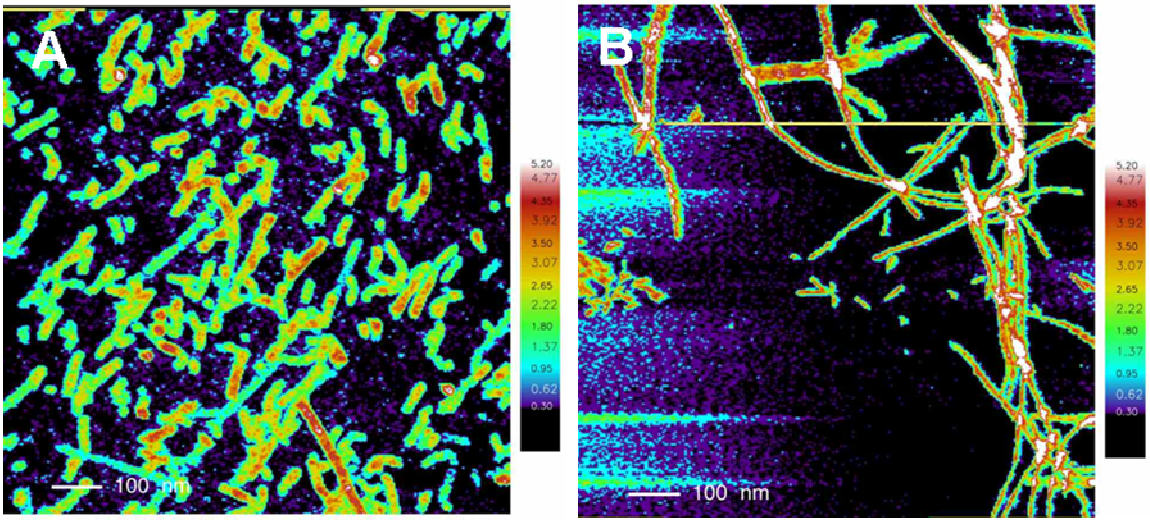

Figure 2.4: Aβ40 (E22Q, D23N) incubated for 3 h (A) or 6 h (B) deposited onto ruby mica at pH 7.4.

2.4 Immunoblot analysis of A β 42 aggregates.

Samples of Aβ42 oligomers (incubated for 6 h at 4° C) and protofibrils (incubated for 6 h at 37° C) were mixed with SDS-PAGE sample buffer, and loaded onto 18% Tris-Gycine polyacrylamide gels (Invitrogen, Carlsbad, CA), electrophoresed and transferred onto Hybond-ECL nitrocellulose membranes (Amersham, Arlinton Heights, IL) at 100 V for 1.5 hour at 4° C. Membranes were blocked in 5% milk/PBS/0.05% Tween20 (PBS-T) for 1 h at RT. Anti-Aβ mouse monoclonal antibody (mAb) 6E10 (Senetek, Napa, CA) was added for 1h at RT, and then washed away 3 x 5 min PBS-T. Horseradish peroxidase-conjugated mouse sheep anti-mouse IgG (1:5000 Amersham-Pharmacia, Piscataway, NJ) was added for 1 h RT, and then washed 3 x 5 min with PBS-T. Bands were visualized using the ECL detection method (Amersham-Pharmacia, Piscataway, NJ). Molecular sizes were determined using Benchmark pre-stained protein ladder (Invitrogen, Carlsbad, CA) and Rainbow molecular weight markers (Amersham Biosciences, Pittsburg, PA)

2.5 Cell Toxicity Assays

Primary mouse neuronal cultures and rat pheochromocytoma (PC12) cells were graciously provided by the Van Nostrand laboratory (Stony Brook University, Stony Brook, NY). Cells in 48-well plates were treated with amyloid peptides (n= 5, final concentration 5 μm peptide) and incubated for 48 h. The cells were then tested for mitochondrial activity. MTT, 3-(4,5-dimethylythiazol-2-yl)2,5-diphenyltetrazolim bromide (CGD-1 kit, M-0283,Sigma-Aldrich), was added at a final concentration of 0.5mg/ml, and the cells were incubated for 4 hours. To determine the cellular reduction of MTT to MTT formazan, the reaction was terminated by addition of 200μL of a cell

lysis solution, 0.1 N HCl isopropanol solution (Sigma-Aldrich, St. Louis, MO), and the plate was shaken at RT to allow the MTT formazan precipitates to dissolve. The assays were then quantified by measuring the 570 nm absorbance using a Molecular Devices M2 microplate reader.

2.6 Solid-state NMR Analysis

Lyophilized amyloid oligomer and fibril samples were packed into 4 mm rotors and analyzed by solid-state NMR to measure through space contacts between pairs of ^{13}C-labels that were introduced into synthetic peptides of Aβ and PrP(118-135). Measurements were made on either a 360, 600, or 750 MHz Bruker AVANCE spectrometer using 4 mm magic angle spinning (MAS) probes. The MAS spinning rate was set to eliminate overlap of MAS sidebands with ^{13}C cross peaks in the 2D ^{13}C dipolar recoupling measurements. Ramped amplitude cross polarization (34) contact times were 2 ms in all experiments and two-pulse phase-modulated (35) decoupling was used during the evolution and acquisition periods. The decoupling field strength was typically 90 kHz. ^{13}C chemical shifts were referenced to external neat tetramethylsilane. The solid-state NMR samples contained approximately 10-20 mg of peptide. Fibril samples had lower yields than oligomer samples due to the extra pelleting and washing steps during sample preparation.

2D ^{13}C dipolar recoupling measurements were carried out using dipolar-assisted rotational resonance (DARR) (36) with mixing times of 600 ms to maximize homonuclear recoupling between ^{13}C labels (see Figure 2.5)(37). The ^{1}H radiofrequency field strength during mixing was matched to the spinning speed to satisfy the n=1

condition for each sample. Each 2D data set represents 1K to 5K scans in each of 64 – 128 rows in the f1 dimension. 10 Hz of exponential line broadening was used in the f2 dimension and a cosine multiplication was used in the f1 dimension along with a 24-coefficient forward linear prediction. Two dimensional ^{13}C DARR spectra exhibit intense diagonal peaks that corresponds to the one-dimensional ^{13}C spectrum and smaller off-diagonal cross peaks produced by through-space dipolar interactions between ^{13}C-labeled sites (see figure 2.6). The experimentally derived upper limit for observing a DARR contact is ~ 6 Å.

.

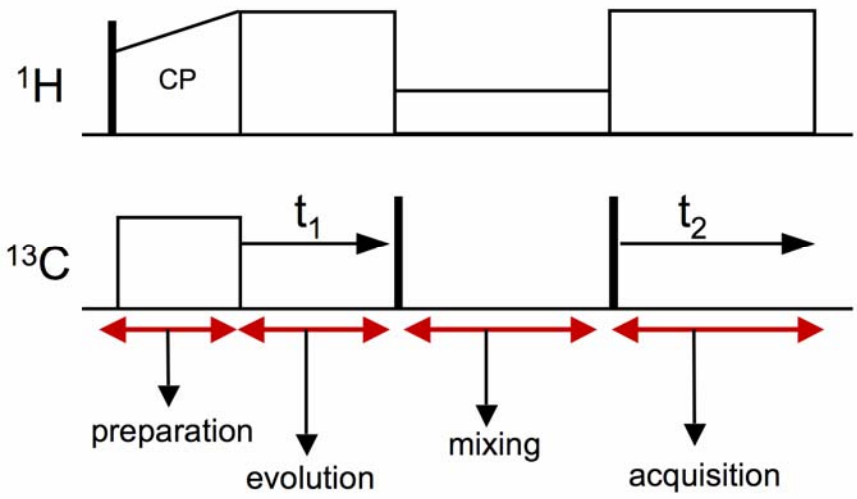

Figure 2.5: A schematic representation of the DARR pulse sequence. The DARR pulse sequence has four parts: preparation of magnetization, evolution of spins, mixing period, where spins are allowed to interact with each other and an acquisition period (38-40)

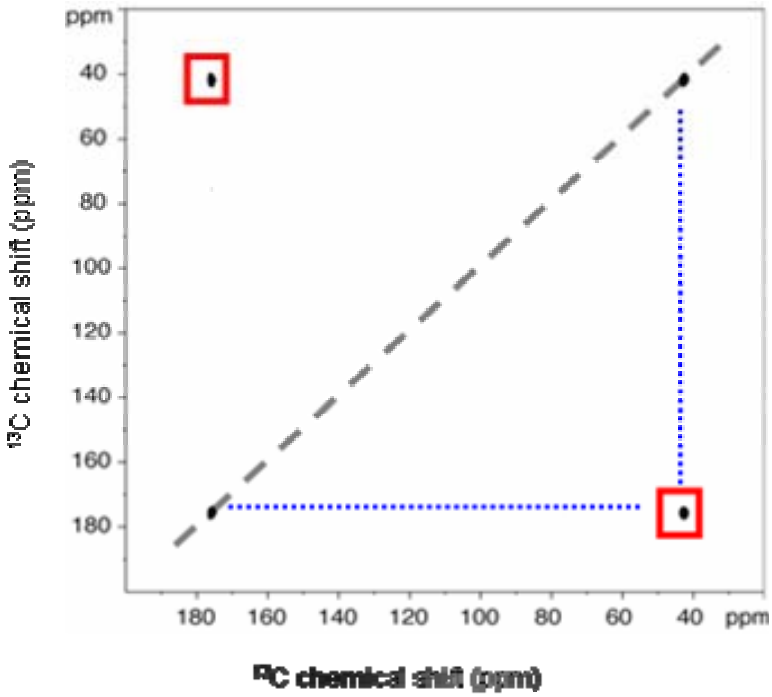

Figure 2.6: Example of a typical DARR spectra used to measure dipolar couplings between distinct pairs of ^{13}C-labels. Intense diagonal peaks corresponds to the one-dimensional ^{13}C spectrum, and smaller off-diagonal cross peaks are produced by through-space dipolar interactions between ^{13}C-labeled sites that are less than 6 Å apart.

Chapter 3

Molecular conformations of amyloid-β(1-42) fibrils and cytotoxic oligomers

3.1 Introduction

One of the major pathological hallmarks of Alzheimer's disease (AD) is the formation of neuritic plaques in the gray matter of AD patients (41). These plaques are composed primarily of filamentous aggregates (fibrils) of the 39-42 amino acid long amyloid-β (Aβ) peptide formed from the proteolytic cleavage of amyloid precursor protein (APP) by β- and γ-secretases (42-44). The major species of Aβ production are the Aβ40 and Aβ42 peptides, with Aβ42 being more predominant in neuritic plaques of AD patients and exhibiting a higher *in vitro* propensity to aggregate and form amyloid fibrils (44-47). Genetic mutations found in familial AD result in an increase in the Aβ42:Aβ40 ratio in cell culture and mouse models (48), and evidence indicates that elevated plasma levels of Aβ42:Aβ40 are correlated with AD (49). Given the pathological significance of the Aβ42 isoform, determining the molecular structure of its fibrils and pre-fibrillar oligomers is crucial for elucidating the folding and aggregation pathway involved in plaque formation and for designing novel therapeutic and diagnostic agents.

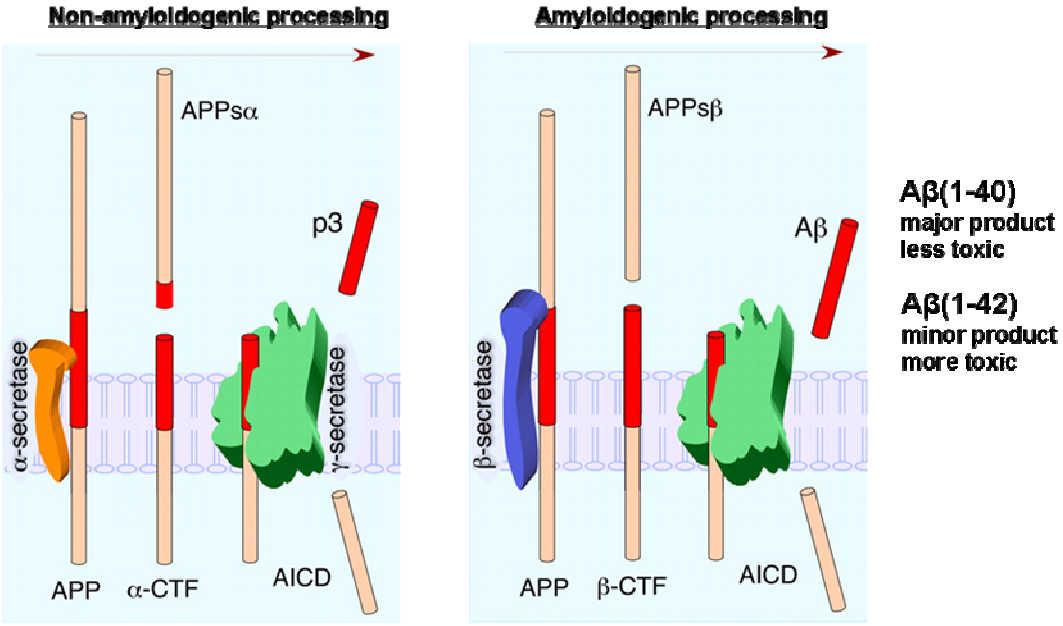

Figure 3.1: Aβ is produced from the proteolytic cleavage of APP by β- and γ-secretases from *Thinakaran et al.* (50).

A number of high-resolution structural studies have been done on fibrils formed from both Aβ42 and Aβ40 (see Table 1). Current understanding of the structure of Aβ42 fibrils is based on solid-state NMR and EPR measurements showing that Aβ42 fibrils have a cross-β structure where individual β-strands polymerize perpendicular to the fibril axis and have a parallel and in-register orientation (51, 52). On the basis of H/D exchange, mutagenesis and cryo-electron microscopy (EM) experiments using recombinant Aβ42 peptides where Met35 is either oxidized (M35Ox) or mutated to Leu (M35L), Lührs *et al.* (53) developed a model of Aβ42 fibrils where residues 1-17 are unstructured and residues 18-42 form a β-strand-turn-β-strand (β-hairpin) motif. The β-strands within the hairpin were found to be staggered relative to one another with Phe19

forming an intra-hairpin contact with Gly38 on adjacent β-hairpin units, and only β-hairpin unit was found at the 4.7 Å cross section of a fibril.

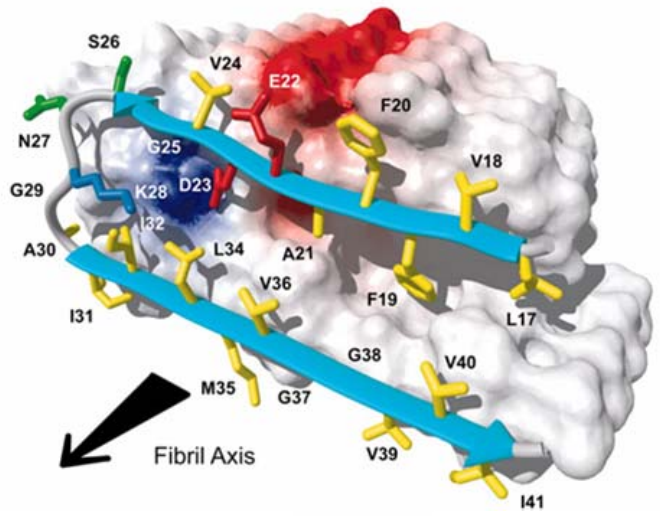

Figure 3.2: Model of Aβ42 fibrils, from *Lührs et al.* (53). Structure was based on hydrogen/deuterium exchange NMR, pair-wise mutagenesis, and cryo-electron microscopy using Met35Ox or M35L peptides.

A different model of Aβ40 fibrils was developed by Tycko and coworkers based on solid-state NMR using synthetic Aβ40 peptides. According to their model of Aβ40 fibrils, residues 1-10 are unstructured and residues 11-40 form a staggered β-hairpin unit with a different set of intra-hairpin contacts between Leu17/Phe19 and Ile32/Leu34/Val36 and between Gln15 and Val36 (54). In addition, two beta-hairpin units were found at the 4.7A cross section of Aβ40 fibrils, with inter-hairpin contacts between Met35 and Gly33 and between Ile31 and Gly37. Questions remain as to whether these observed structural differences are a result of the different peptides and biophysical methods used.

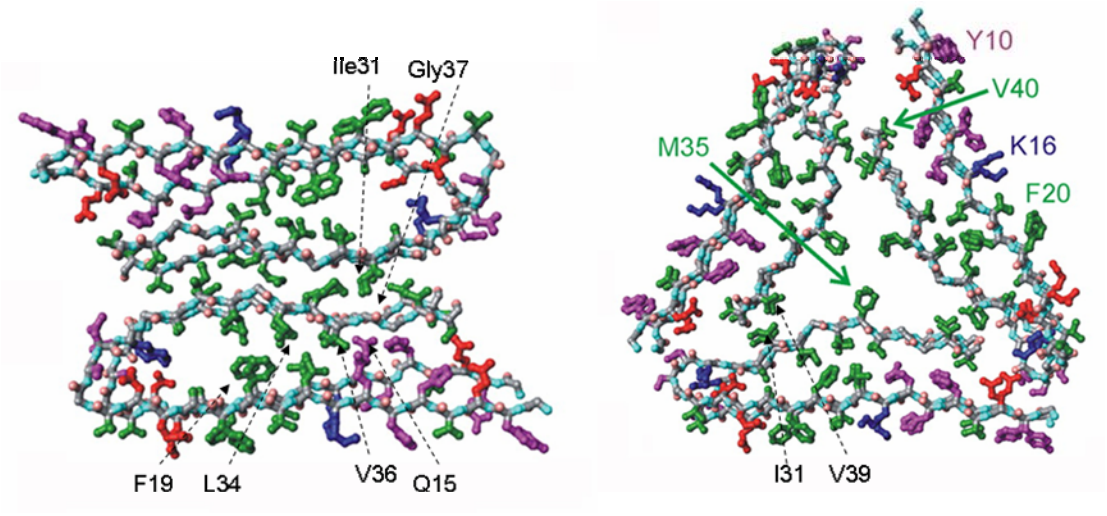

Figure 3.3: Models of Aβ40 fibril polymorphs, from *Tycko* (10) and *Paravastua et al.* (11). Different molecular contacts are observed in fibrils grown under shaken conditions (left) or from a progressive seeded preparation (right). Measurements were based on 13C solid state NMR measurements by Tycko and co-workers (54).

Considerably less is known about the molecular structure of Aβ pre-fibrillar soluble oligomers. Oligomeric forms of Aβ have been shown to cause neuronal dysfunction (55-57), disrupt long term potentiation (58), and cause memory impairments in mouse models of AD (59). A growing body of literature has implicated the pre-fibrillar oligomers and not the fibrillar form as the primary pathological species of AD (60, 61). Of particular pathological significance is the Aβ42 isoform. Low-level expression of Aβ42, versus over-expression of Aβ40, has been shown to correlate with extensive amyloid pathology in transgenic mouse models (62). Reports have also shown that the pre-fibrillar form of Aβ42, unlike Aβ40, can form stable SDS-resistant trimeric/tetrameric complexes (63) or stable pentameric/hexameric building blocks, as shown by photo-oxidative crosslinking (64). While no high resolution structural models of Aβ42 oligomers are available, efforts have been made with Aβ40. Ishii and co-

workers (27) have used solid-state NMR and EM to show that a 15-35 nm toxic intermediate of Aβ40 oligomers have fibril-like β-sheet structures. Given the differences in both toxicity and stability between Aβ42 and Aβ40 oligomers, high resolution structural data of Aβ42 oligomers has become of great interest.

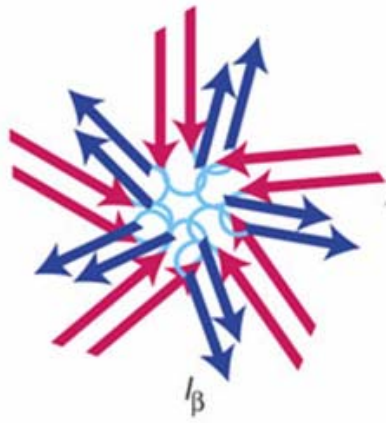

Figure 3.4: Schematic of a toxic spherical Aβ40 oligomer intermediate, *from Chimon et al.* (27). Oligomers contain 200-400 monomer units, have diameters of 15-35 nm, and have parallel beta-sheet structures.

In order to more accurately characterize the high resolution structures of both fibrils and pre-fibrillar oligomers of Aβ42, Transmission electron microscopy (TEM), single-touch atomic force microscopy (AFM), and solid-state NMR measurements were utilized on a series of Aβ42 peptides with specific ^{13}C labels in the hydrophobic core region at His13, His14, Gln15, Phe19, Ile31, Gly33, Met35, Gly37, Val39, and Ala42 (see Table 3.2). The analysis led to defined molecular contacts in both the oligomeric and fibrillar conformations of Aβ42 and a better understanding of the structural transitions involved in aggregation and toxicity.

Table 3.1: Previous high-resolution structural data of Aβ42 and Aβ40 fibrils and oligomers

	Aβ42	Aβ40
Fibrils	Residues 1-17 unstructured; residues 18-42 form β-hairpin unit with intra-hairpin contacts between Phe19 and Gly38 (53) β-strands are parallel and in-register (51, 52), and are staggered within the hairpin (53) One hairpin unit per 4.7 Å cross-section (53) C-terminal β-strand breaks at Gly37/Gly38 to allow Ala42 to make contact with Met35 (65)	Residues 1-10 unstructured; residues 10-40 form β-hairpin unit with intra-hairpin contacts between Phe19 and Ile32/Leu34/Val36 β-strands are parallel and in-register (51, 52), and are staggered within the hairpin (10) Two β-hairpin units per 4.7 Å cross-section with inter-hairpin contacts between Met35 and Gly33 and between Ile31 and Gly37 (66) Specific polymorph has 3 β-hairpin units per 4.7 Å cross-section (11)
Oligomers	none	Toxic intermediate (15-35 nm) has parallel β-sheets (27)

Table 3.2: Isotope labeled Aβ42 peptides.

Aβ42-HQA	$^{13}C\varepsilon_1$-His13, $^{13}C\varepsilon_1$-His14, $^{13}C\delta$-Gln15, $^{13}C\gamma$-Ala42
Aβ42-FLG	ring-$^{13}C_6$-Phe19, U-$^{13}C_6$,^{15}N-Leu34, $^{13}C\alpha$-Gly38
Aβ42-M35	$^{13}C\varepsilon$-Met35
Aβ42-G33	$^{13}C\alpha$-Gly33
Aβ42-G37	$^{13}C\alpha$-Gly37
Aβ42-GMG	^{13}CO-Gly33, $^{13}C\varepsilon$-Met35, $^{13}C\alpha$-Gly37
Aβ42-I31	U-$^{13}C_6$,^{15}N-Ile31
Aβ42-V39	U-$^{13}C_5$,^{15}N-Val39

3.2 Characterization of Aβ42 neurotoxic oligomers and fibrils.

Samples of Aβ42 oligomers, protofibrils and mature fibrils were verified using TEM and AFM. Aβ42 oligomers were prepared at low temperature and low salt conditions (200 μM Aβ, 4°C, 10 mM phosphate, 10 mM NaCl, pH 7.4). TEM analysis showed that under these conditions, the oligomeric sample contains a nearly homogeneous sample of round oligomers with average widths of ~10-15 nm (Figure 3.5A, 3.6B). Single-touch AFM was used to probe the fine structure of these oligomers (Figure 3.5D, Supplementary Figure 3.6A). Oligomers appear wider in AFM images due to the width of the scanning tip (see Methods). AFM analysis showed that the oligomeric samples contain particles having corrected widths of 10-15 nm and heights of ~2-4 nm, and a smaller subset of particles with corrected widths of 5-7 nm and heights of ~1 nm. When Aβ42 peptides were incubated for short periods (6 h at 37°C), the oligomers became more narrow and elongated into protofibrils (Figure 3.5B). Mature fibril samples were formed after 12

days of incubation at 37°C under physiological salt conditions (200 μM Aβ, PBS, pH 7.4). TEM analysis was used to show that fibrils were extensively long and formed dense networks (Figure 3.5C).

To characterize the early stages of aggregation and toxicity, immunoblot analysis and neuronal cell toxicity assays were used to characterize the nature of the oligomeric and protofibril samples (Figure 3.5E, 3.5F). Using the anti-Aβ mouse monoclonal antibody (mAb) 6E10, we show that the oligomeric sample contains SDS-resistant trimers and tetramers along with unaggregated monomer. The protofibril sample displayed an additional smear of aggregates >25 kDa. The toxicities of oligomeric and protofibril samples were tested by treating primary mouse cortical neurons with either oligomers or protofibrils (5μM Aβ final concentration) and measuring mitochondrial activity 48 h post treatment. Oligomeric samples displayed significantly higher toxicity than protofibril samples with $p<0.02$.

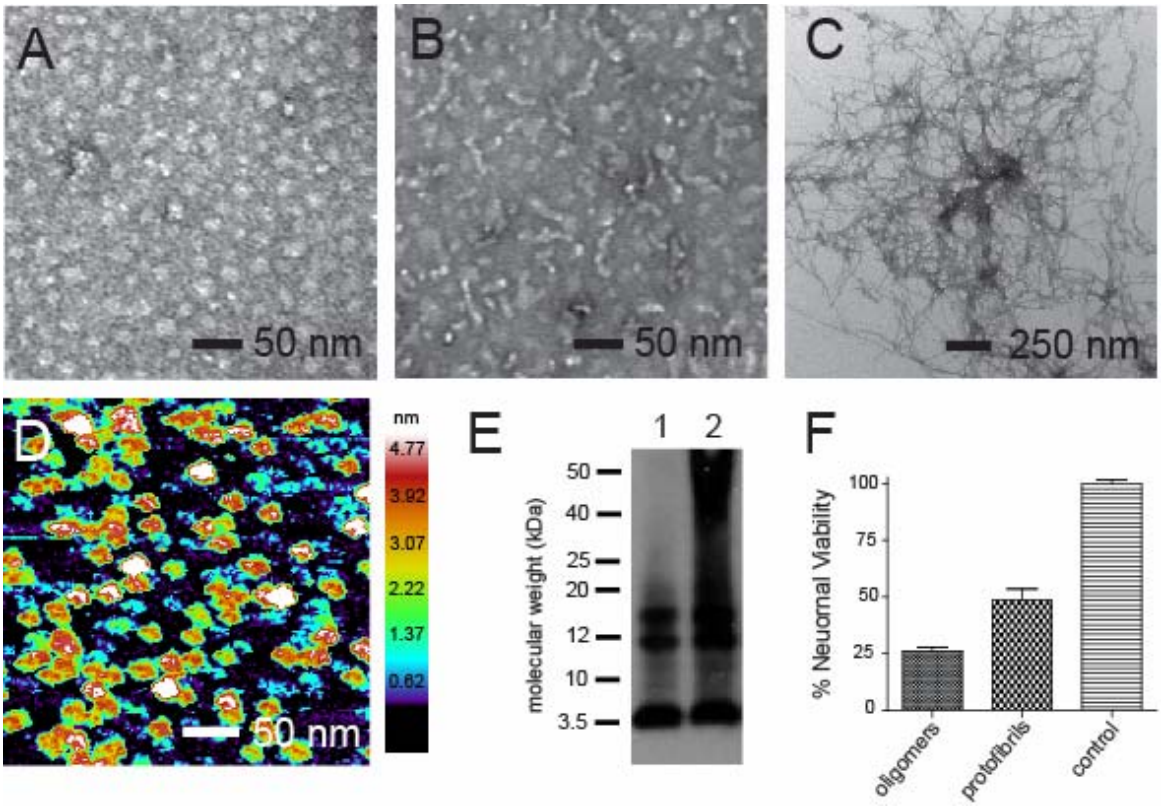

Figure 3.5: Characterization of Aβ42 neurotoxic oligomers and fibrils. (A) TEM of Aβ42 oligomers incubated at 4°C for 6h. (B) TEM of Aβ42 protofibrils incubated at 37°C for 6h. (C) TEM of Aβ42 fibrils incubated 37°C for 12 d. (D) Single-touch AFM of Aβ42 oligomers. (E) Immunoblot analysis of Aβ42 oligomers (lane 1) and protofibrils (lane 2) using anti-Aβ mouse monoclonal antibody (mAb) 6E10. (F) MTT cell viability assay of primary mouse cortical neurons treated with Aβ42 oligomers or protofibrils.

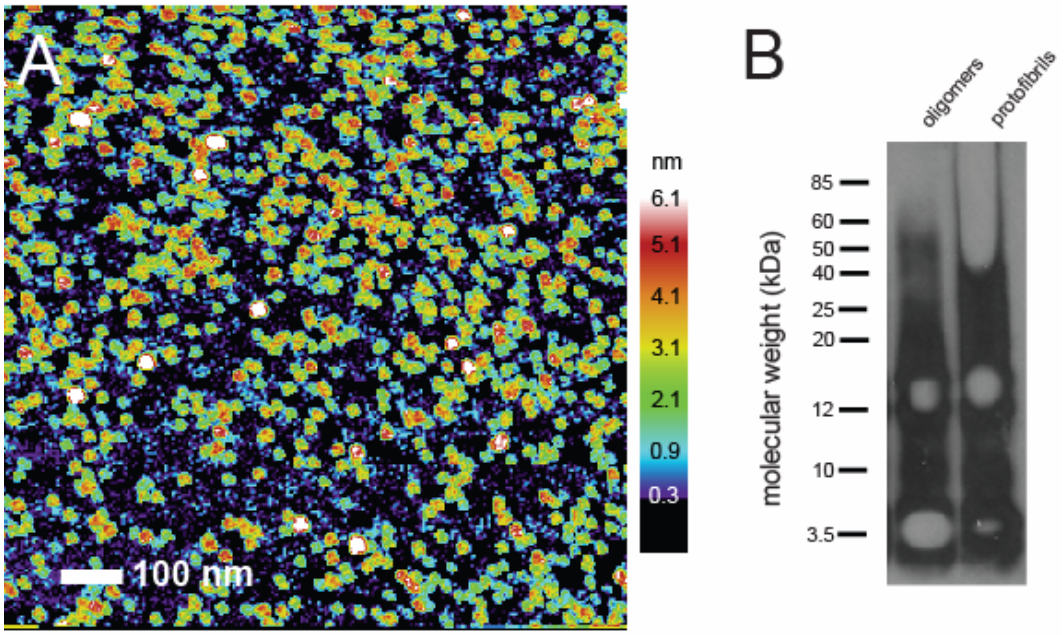

Figure 3.6: AFM and Immunoblot analysis of Aβ42 oligomers. (A) AFM image of a 1-micron field view of Aβ42 oligomers. The majority of particles have corrected width of 10-15 nm and heights of ~2-4 nm. (B) Over-exposed immunoblot of Aβ42 oligomers and protofibrils. The largest band indicates the presence of a 56 kDa species corresponding to a dodecamer.

3.3 Fourier Transform Infrared Spectroscopy of Aβ42

FTIR transmission spectra were obtained of Aβ42 oligomers as a function of time on a Bruker IFS 66V/S spectrometer. Several groups have previously demonstrated that there are significant batch-to-batch differences in the ability of synthetic Aβ peptides to adopt β-sheet secondary structure (67, 68). The most toxic Aβ peptides are those that rapidly convert to β-sheet when dissolved in aqueous solution (67). FTIR data is presented to demonstrate that our synthetic Aβ42 peptides are capable of rapidly forming β-secondary structure. The amide I region of the Aβ42 peptide after 0.5 - 24 h of incubation at 25°C is shown in Figure 3.7. The observation of a resolved band at 1630 cm^{-1} demonstrates that β-sheet secondary structure rapidly forms. It is more difficult to distinguish α-helix from random coil in IR since both exhibit amide I vibrations in the region of ~1650-1660 cm^{-1} (69). The broad component at 1660 cm^{-1} is interpreted as random coil based on the clear observation of a negative 200 nm CD band at early times (70). Moreover, random coil characteristically yields a broad amide I band (full width at half max > 50 cm^{-1}), as observed, rather than a sharp Lorentzian lineshape (full width at half max < 40 cm^{-1}) characteristic of defined helical (or β-sheet) secondary structure. The data indicate oligomer and protofibril samples contain significant β-content.

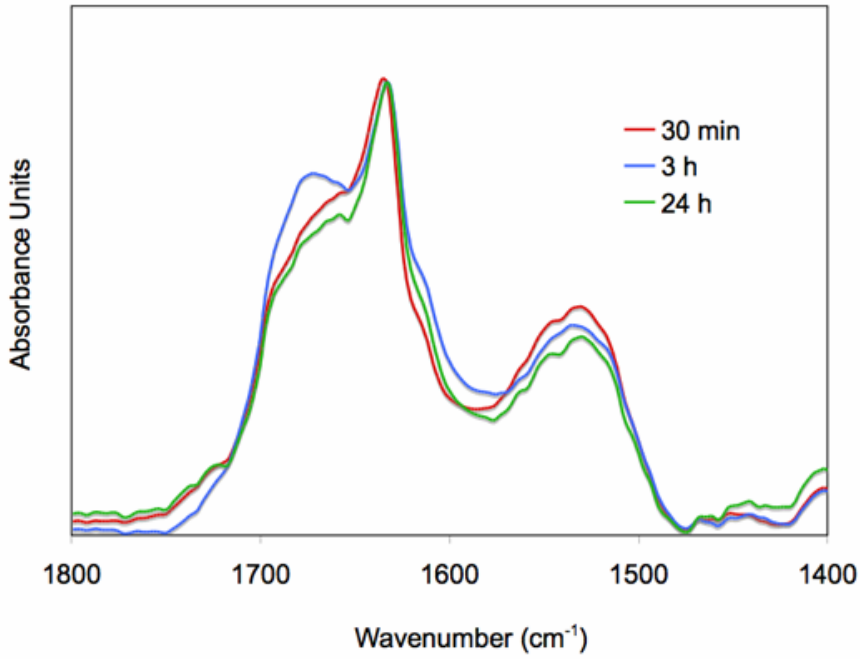

Figure 3.7: FTIR of Aβ42 soluble oligomers. Pure Aβ42 peptide was incubated at a concentration of 40 μM at 25 °C for 30 min (red), 3 h (blue), and 24 h (green). The sample was layered onto germanium IR plates and bulk solvent was removed. Transmission spectra were obtained with 2 cm−1 resolution from 500–4000 cm−1. Only the amide I region of the IR spectrum is shown.

3.4 Investigation of β-hairpin structures in fibrils and neurotoxic oligomer

The initial effort was to establish the side chain packing within the β-hairpin structure of Aβ42 fibrils, and whether a similar structure can be observed in Aβ42 oligomers. Specifically we wanted to address whether Phe19 packs against Gly38 as predicted by the model of Aβ42 fibrils by Luhrs et al.(53) using mutagenesis studies of Aβ42(M35L) peptides or whether Phe19 packs against Leu34 as measured in Aβ40 fibrils by solid state NMR (10). A specific method of ^{13}C solid-state NMR spectroscopy, dipolar assisted rotational resonance (DARR), was used to measure $^{13}C...^{13}C$ dipolar couplings within a single Aβ42 peptide containing ring-$^{13}C_6$-Phe19, uniformly (U)-$^{13}C_6$,^{15}N-Leu34, and $^{13}C\alpha$-Gly38, referred to as Aβ42-FLG. Dipolar couplings are seen as off-diagonal crosspeaks in two dimensional DARR spectra and indicate molecular contacts that are less than 6 Å apart (see Methods). The DARR experiment (Figure 3.8A) shows molecular contacts between ring-carbons (Cδ1, Cδ2, $C\varepsilon_1$, $C\varepsilon_2$, Cζ) of Phe19 and side-chain carbons (Cγ, $C\delta_1$, and $C\delta_2$) of Leu34. No contacts were observed between Phe19 and Gly38. The data indicate that the intra-hairpin side-chain packing of Aβ42 fibrils closely resembles the intra-hairpin side chain packing of Aβ40 fibrils.

The next investigation was to determine whether this specific β-hairpin conformation exists in the Aβ42 oligomers using the same Aβ42-FLG peptide. The DARR spectra (Figure 3.8B) shows that in oligomeric Aβ42, all of the ring carbons (Cγ, Cδ1, Cδ2, $C\varepsilon_1$, $C\varepsilon_2$, Cζ) of Phe19 make contact with all of the side-chain carbons (Cβ, Cγ, $C\delta_1$, and $C\delta_2$) of Leu34. The additional cross-peaks in the oligomer sample are likely due to the higher sensitivity of oligomeric versus fibril NMR samples (see Methods). Because of chemical shift overlap between the Cα of Gly38 and the Cβ of Leu34, we

could not rule out the possibility that Phe19 makes also make a contact with Gly38 in Aβ42 oligomers. The contact between Phe19 and Leu34 indicates that Aβ42 fibrils and oligomers have a similar β-hairpin structure (Figure 3.8C).

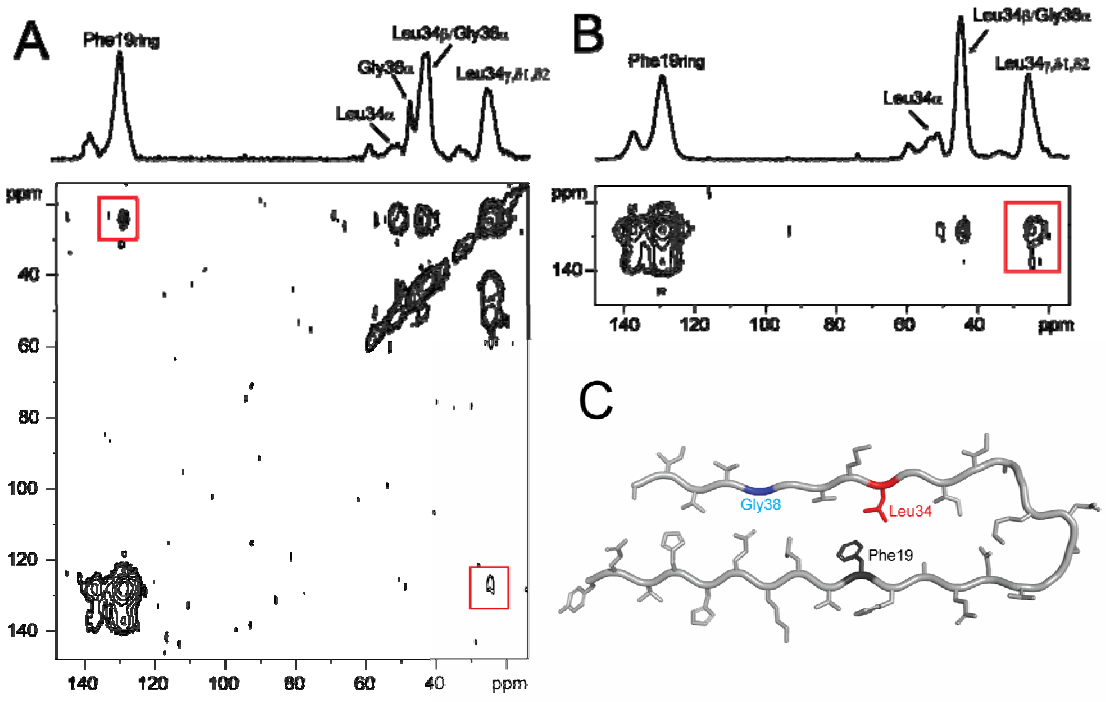

Figure 3.8: Phe19 packs against Leu34 in Aβ42 fibrils and oligomers. (A) Above, 1D 13C-spectra showing chemical shift assignments for Phe19, Leu 34, and Gly38 in Aβ42 fibrils formed form Aβ42-FLG peptides. Below, 2D DARR spectra showing specific 13C…13C molecular contacts between Phe19 and Leu34 (red box). No contact was observed between Phe19 and Gly38. (B) Above, 1D 13C-spectra showing chemical shift assignments for Phe19, Leu 34, and Gly38 in Aβ42 oligomers formed form Aβ42-FLG peptides. Below, slice from 2D DARR spectra showing specific 13C…13C contact between Phe19 and Leu34 in Aβ42 oligomers. Because of chemical shift overlap between Gly38 and Leu34 in the oligomeric state, a Phe19-Gly38 contact in Aβ42 oligomers could not be ruled out, but is not likely given the large relative crosspeak between Phe19 and the Cγ,Cδ1,and Cδ2 of Leu34 (red box). (C) Molecular model of β-hairpin conformation of Aβ42 peptides found in both fibrils and oligomers.

3.5 Investigation of parallel and in-register orientation of β-strands in fibrils and neurotoxic oligomers

To verify that the Aβ42 fibrils used in this study were composed of β-strands that have polymerized in a parallel and in-register orientation (Figure 3.9B), Gly33 was used as a probe to measure inter-strand $^{13}C\ldots^{13}C$ dipolar couplings. We prepared fibrils samples consisting solely of Aβ42-GMG peptides or an equimolar mixture of Aβ42-GMG:Aβ42-G33 peptides (see Table 3.2). Figure 3B shows the 1 dimensional row of the DARR crosspeak observed between carbonyl carbon (CO) of Gly33 and the Cα of Gly33 of an adjacent peptide in the Aβ42-GMG:Aβ42-G33 sample relative to the natural abundance crosspeak observed in the Aβ42-GMG alone sample. Natural abundance crosspeaks arise in DARR experiments from directly bonded carbon atoms (CO and Cα) due to 1.1% natural abundance of ^{13}C. This direct inter-strand contact between Gly33 residues on adjacent peptides indicates that the beta-strands have an in-register orientation.

We then tested the same labeling scheme in the oligomeric Aβ42 sample (Figure 3.9C). In contrast to the fibril sample, no significant crosspeak was observed relative to natural abundance. This indicates that the β-hairpin units in Aβ42 oligomers are not perfectly in-register and are likely in an alternate configuration.

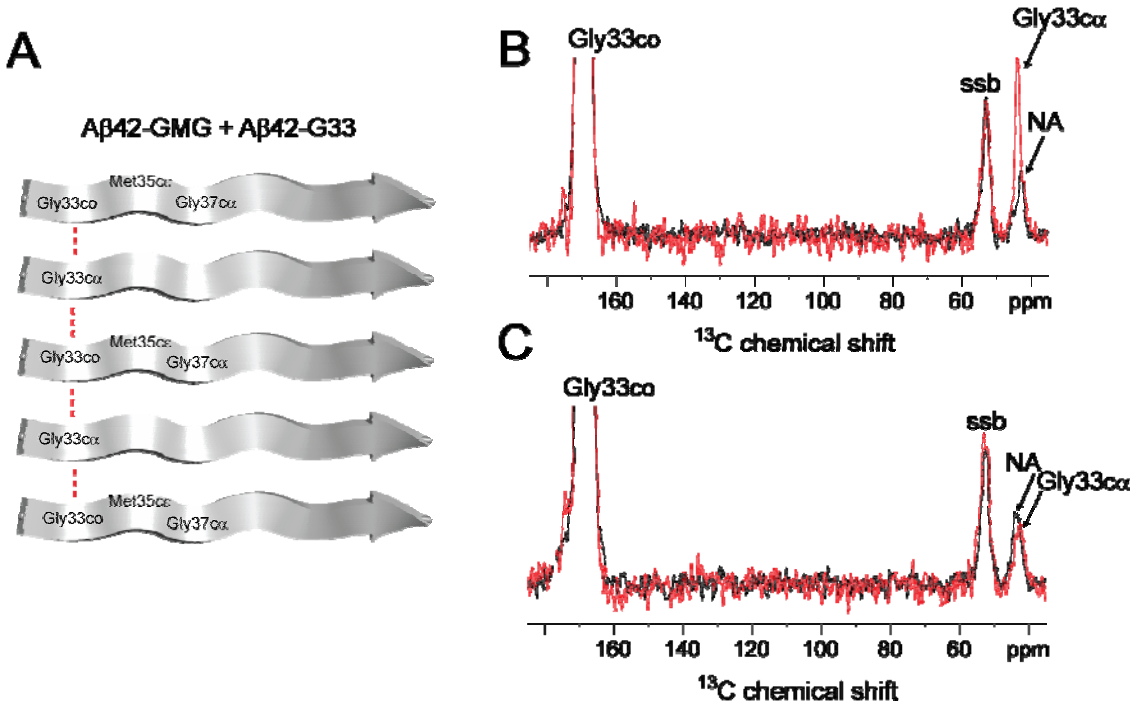

Figure 3.9: Aβ42 fibrils have a parallel and in-register orientation; stable oligomers do not. (A) Labeling scheme to test in-register orientation of β-strands in Aβ42 fibrils and oligomers using an equimolar mixture of Aβ42-GMG:Aβ42-G33 peptides to detect interstrand contacts along the fibril length at the Gly33 position. (B) Row through Gly33-CO chemical shift from 2D DARR spectra of Aβ42 fibrils formed from an equimolar mixture of Aβ42-GMG:Aβ42-G33 peptides (red trace) or Aβ42-GMG peptide alone (black trace). A large cross peak relative to natural abundance (NA) is observed in the Aβ42-GMG:Aβ42-G33 sample indicating interstrand molecular contacts between Gly33-CO and Gly33-Cα in a parallel an in-register orientation. (C) Row through Gly33-CO chemical shift from 2D DARR spectra of Aβ42 oligomers formed from an equimolar mixture of Aβ42-GMG:Aβ42-G33 peptides (red trace) or Aβ42-GMG peptide alone (black trace). No contact was observed between Gly33-CO and Gly33-Cα, indicating that Aβ42 oligomers do not likely have a parallel and in-register orientation.

3.6 Investigation of β-strand staggering in fibrils and neurotoxic oligomers

The β-strands within the β-hairpin motif have previously been shown to have a staggered conformation in both Aβ42 (53) and Aβ40 (10). To examine the exact side-chain registry of this domain swapping feature, we first prepared fibril samples using an equimolar mixture of Aβ42-HQA:Aβ42-G37 to measure $^{13}C\ldots^{13}C$ dipolar couplings between Gln15 and Gly37 on adjacent peptides. The DARR measurements (Figure 3.10A) show that side-chain carbon (Cδ) makes contact with the backbone carbon (Cα) of Gly37. This contact is consistent with the side chain packing registry predicted from our Phe19-Leu34 intra-hairpin contact and the recent report of a Gln15-Val36 contact observed in Aβ40 fibrils (11). A DARR contact was also observed between the Cδ of Gln15 and the Cε of His13/14, which indicates that His13/14 and Gln15 lie in an ordered β-strand domain. Both of these points are contrary to the notion that all of the residues 1-17 of Aβ42 fibrils are disordered proposed by Luhrs et al. (53).

The analogous experiment was then tested on Aβ42 oligomers using an equimolar mixture of Aβ42-HQA:Aβ42-G37 peptides (Figure 3.10B). No DARR contacts were observed between Gln15 and Gly37. The lack of a domain-swapped Gln15-Gly37 contact in Aβ42 oligomers is consistent with the absence of a parallel and in-register orientation previously shown in Figure 3.10. The data indicates that Aβ42 oligomers are significantly less ordered than the tightly packed parallel and in-register fibrils.

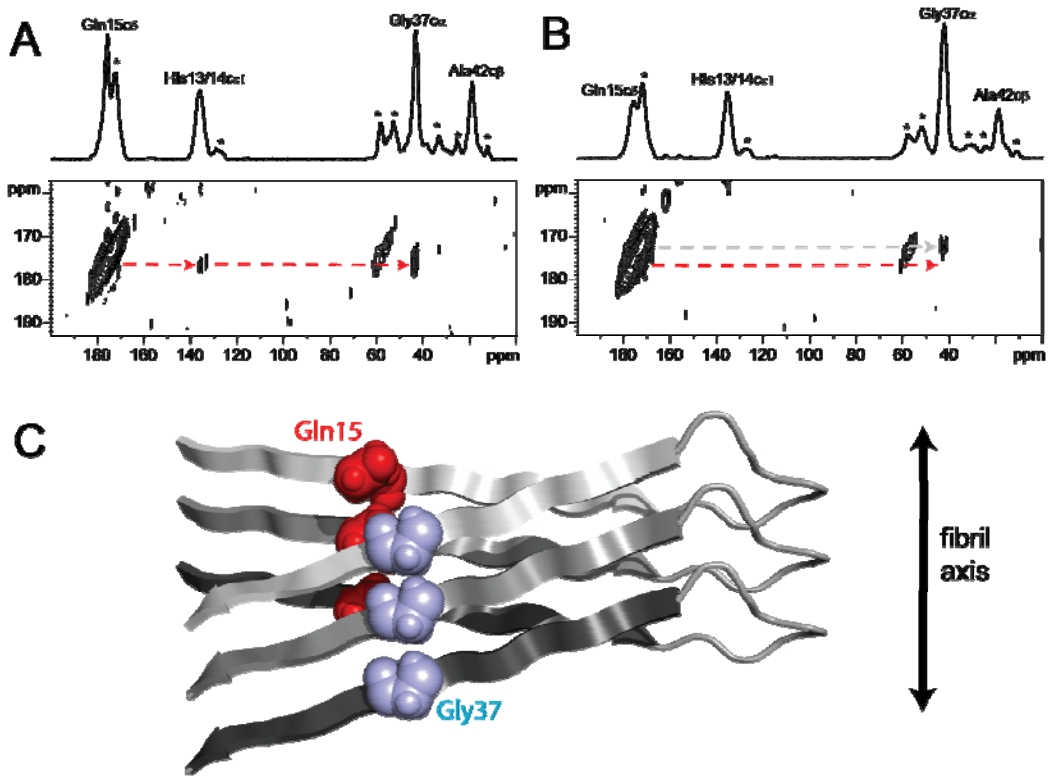

Figure 3.10: Gln15 forms domain-swapped contact with Gly37 in Aβ42 fibrils, but not in oligomers. (A) 1D 13C-spectra showing chemical shift assignments for His13/14, Gln15, Gly37,and Ala42 in Aβ42 fibrils formed from an equimolar mixture of Aβ42-HQA:Aβ42-G37 peptides. Below, slice of 2D DARR spectra showing specific 13C…13C intermolecular contacts between Gln15 and Gly37 and intra-molecular contacts between His13/14 and Gln15 (red arrows), indicating a staggered domain-swapped architecture. No contacts were observed between Gln15 and Ala42. (B) 1D 13C-spectra showing chemical shift assignments for His13/14, Gln15, Gly37,and Ala42 in Aβ42 oligomers formed from an equimolar mixture of Aβ42-HQA:Aβ42-G37 peptides. Below, slice of 2D DARR spectra showing no molecular contacts between Gln15 and His13/14, Gly37, or Ala42 (red arrow), indicating the absence of a staggered domain swapped architecture in Aβ42 oligomers. A small natural abundance crosspeak is observed (gray arrow) due to the higher sensitivity of the oligomeric samples. (C) Model of Aβ42 fibrils with staggered β-strands based on Gln15 – Gly37 domain swapped contact.

3.7 Conformation of Met35 and higher order structural features in fibrils and neurotoxic oligomers.

To investigate the possibility of higher order arrangements of the β-hairpin units in Aβ42 fibrils and neurotoxic oligomers, C-terminal β-strand residues facing external to the β-hairpin were probed using ^{13}C labels at Ile31, Gly33, Met35, Met37, and Val39. We had previously observed DARR contacts between the Cε of Met35 and Cα of Gly37 in Aβ42 fibrils made from an equimolar mixture of two Aβ42 peptides with ^{13}C-labels at Cε of Met35 or Cα of Gly37 (71). This contact implicated a different β-sheet packing interface for Aβ42 fibrils than the Met35-Gly33 and Ile31-Gly37 packing interface observed in Aβ40 fibrils by Tycko and co-workers (66). To distinguish whether the Met35-G37 contact in Aβ42 fibrils was intermolecular or intramolecular in nature, we synthesized a single Aβ42 peptide labeled at ^{13}CO-Gly33, ^{13}Cε-Met35, ^{13}Cα-Gly37, termed Aβ42-GMG. Our DARR analysis of fibrils grown from Aβ42-GMG revealed that Met35 exists in two conformations as reflected by the splitting in the Met35 resonance at 17.2 and 15.3 ppm (Figure 3.11A). The DARR experiment showed a major contact of the Cε of Met35 (at 17.2 ppm) with the Cα of Gly37, and a minor one of the Cε of Meet35 (15.3 ppm) with the CO of Gly33. Isotopic dilution experiments showed no significant decrease in crosspeak intensities (data not shown), indicating that the Met35 contacts with Gly33 and Gly37 are intra-molecular in nature. The analogous experiment was done on oligomers prepared from Aβ42-GMG peptides (Figure 3.11B). Unlike the fibril sample, Cε of Aβ42 oligomers had a single broad resonance at 15.4 ppm. The same intra-molecular contacts between Met35 and Gly33/Gly37 were observed in oligomeric samples (data not shown). This may indicate that the previously observed contact was of a different fibril polymorph. Other possible inter-hairpin contacts were tested, including the Ile31 – Gly37 contact, previously observed in Aβ40 fibrils (66). No contacts were found in either fibrils or oligomer samples (Figure 3.12).

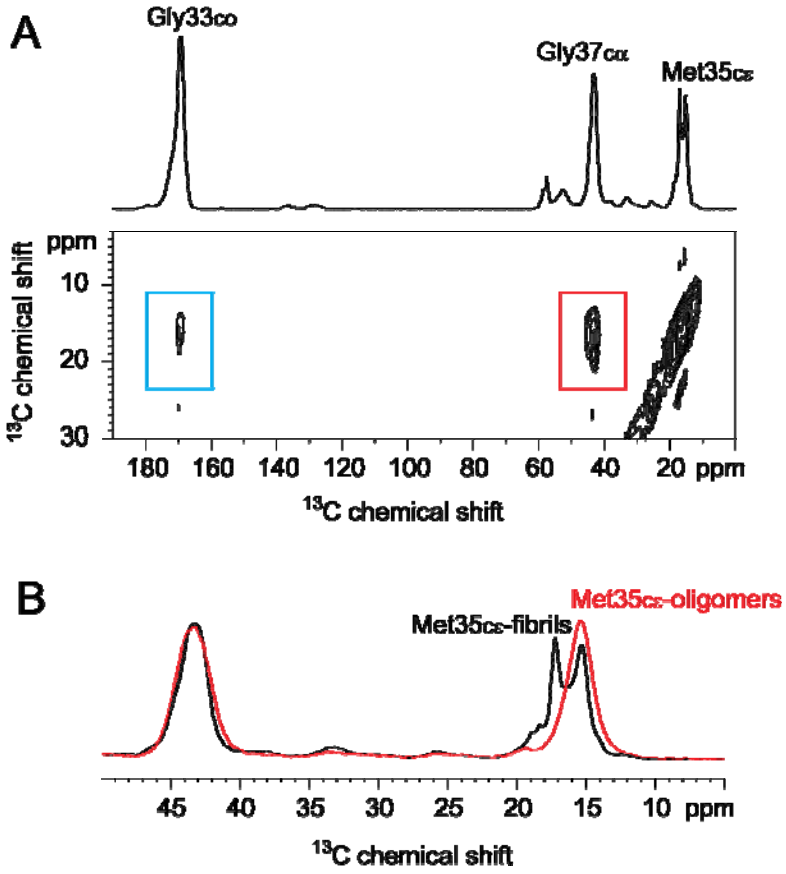

Figure 3.11: Met35 has two conformations that make intra-molecular contacts with Gly33 and Gly37 in fibrils. Met35 has single conformation in oligomers. (A) Above, 1D 13C-spectra showing chemical shift assignments for Gly33, Met35, and Gly37 in Aβ42 fibrils formed from Aβ42-GMG peptides. Below, slice from 2D DARR spectra showing specific 13C…13C molecular contacts between Met35 with both Gly33 (blue box) and Gly37 (red box). Isotopic dilution revealed that both contacts are intra-molecular in nature. (B) 1D 13C-spectra showing Met35 chemical shift assignments of Aβ42 fibrils (black trace) and oligomers (red trace) formed from Aβ42-GMG peptides. Data shows that Met 35 adopts two distinct conformations in the fibril state and a more heterogeneous conformation in the oligomeric state.

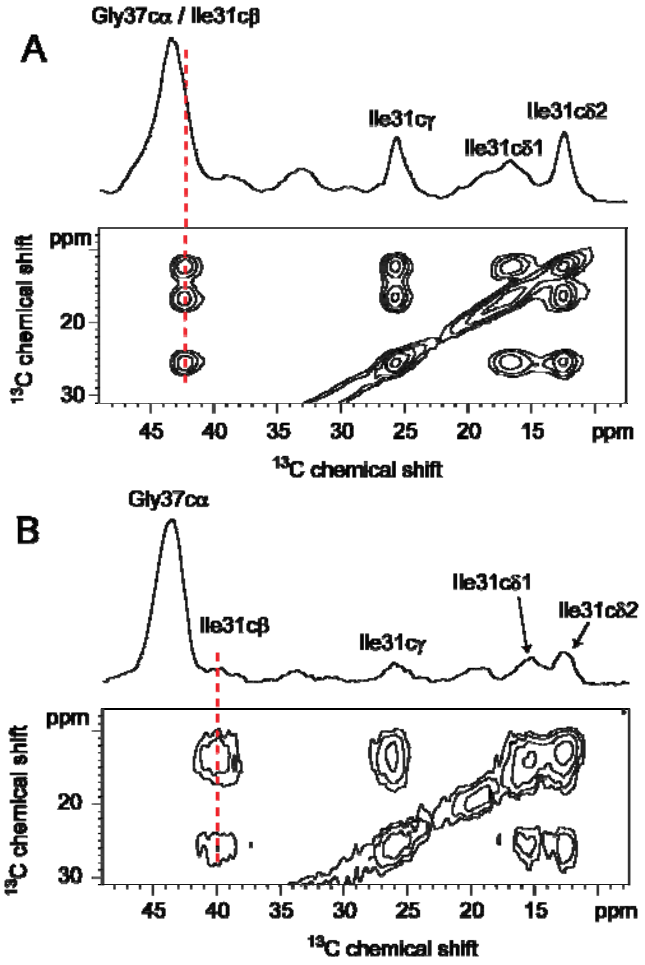

Figure 3.12: Ile31 and Gly37 do not make intermolecular contacts in fibrils nor in oligomers. (A) Above, 1D 13C-spectra showing chemical shift assignments for Ile31 and Gly37 in Aβ42 fibrils formed form an equimolar mixture of Aβ42-Ile31:Aβ42-Gly37 peptides. Below, 2D DARR spectra showing no molecular contacts between Ile31 and Gly37. (B) Above, 1D 13C-spectra showing chemical shift assignments for Ile31 and Gly37 in Aβ42 oligomers formed form an equimolar mixture of Aβ42-Ile31:Aβ42-Gly37 peptides. Below, 2D DARR spectra showing no molecular contacts between Ile31 and Gly37 in Aβ42 oligomers. Note the large chemical shift change in the Cβ of Ile 37 between the oligomeric and fibrillar states.

3.8 *Conformation of Aβ42 fibrils.*

The data along with previous studies of Aβ fibrils indicate that the hydrophobic core of Aβ42 fibrils is composed of a β-strand-turn-β-strand (β-hairpin) motif composed of domain-swapped, parallel and in-register β-sheets. The measurements specifically show that the side-chain packing registry along the internal face of the β-hairpin involves molecular contacts between Phe19 and Leu34 and between Gln15 and Gly37. We also show that the Gln15-Gly37 contact is intermolecular and arises from a staggering of the β-strands within the β-hairpin. Where this model differs from the one proposed by Lührs *et al.* (53) is in the specific side-chain packing registry. According to their model, Phe19 packs against Gly38 based on fibril recovery experiments using a pair-wise mutagenesis strategy. They found that the single G38F or F19G mutations would reduce the fibril-forming capacity of recombinant Aβ42(M35L) peptides, and that the double G38F, F19G mutation would recover fibril forming capacity, implying that Phe19 packs against Gly38. This data show that there is a 4-residue shift in registry where Phe19 packs against Leu34, and we specifically show that Leu34 does not make contact with Gly38 in fibrils formed from synthetic Aβ42 wild-type peptides. It should be noted that the model presented by Lührs *et al.* (53) is based on the use of recombinantly expressed peptides where Met35 is oxidized or mutated to leucine. A number of reports have shown that oxidation of Met35 greatly affects the aggregation and conformation of Aβ fibrils (72-74). The use of synthetic peptides in our experiment allowed us to characterize wild-type Aβ42 peptides where the oxidation state of Met35 can be monitored by chemical shift analysis using our Aβ42-M35 peptide. Under all of the conditions of these experiments, Met35 remained in the reduced state. In addition our data show that Gln15 is part of an ordered β-strand domain, which is inconsistent with the proposal that residues 1-17 of Aβ42 are unstructured (53). It should, however, be noted that the data of residues 1-17

being unstructured was based on H/D exchange experiments where no data could be collected on His14 or Gln15. The side chain packing registry within the β-strand-turn-β-strand motif of Aβ42 fibrils agrees with the F19/I32, F19/L34, F19/V36, Q15/V36 molecular contacts observed in Aβ40 fibrils by Tycko and co-workers (10, 11). These results indicate that the core β-strand-turn-β-strand motif of fibrils formed from Aβ40 and Aβ42 peptides are very similar.

In addition to investigating the side chain packing registry within the β-hairpin motif of Aβ42 fibrils, the possible side chain packing along the external face of the C-terminal β-strand were also investigated. The data showed that the side-chain of Met35 has two distinct conformations that make intramolecular contacts with Gly33 and Gly37. Additionally, no molecular contacts were observed between Ile31 and Gly37, a contact observed by Tycko and co-workers in Aβ40 fibrils (66). Interestingly, the analysis shows that the chemical shift of Cα of Gly37 partially overlaps with the Cβ of Ile31 in the fibril state (see SI Figure S2). This chemical shift overlap is only seen in the fibril state and not seen in the oligomeric state, and can lead to interpreting Ile-Ile intramolecular contacts as Ile-Gly intermolecular contacts. Additionally, no contacts were observed between Gly33 and Val39 (data not shown). The data indicates that the two-fold symmetry of β-hairpin units reported in Aβ40 fibrils does not exist in Aβ42 fibrils. It is likely that Aβ42 fibrils in the non-oxidized state exist as one beta-hairpin unit per 4.7 Å cross-section as predicted by the cryo-EM measurements of Aβ42(M35Ox) fibrils by Luhrs et al., or that an alternative ultra-arrangement exists.

3.9 Conformation of Aβ42 oligomers: implications for toxicity and fibril nucleation

In this investigation of Aβ42 oligomers, it was shown that under low salt and low temperature conditions, a nearly homogeneous mixture of oligomers can be prepared. AFM images showed that the majority of these oligomers have widths of 10-15 nm and heights of 2-4 nm. Previous reports have shown that unlike Aβ40, Aβ42 can form stable oligomers that were found to be trimeric/tetrameric on SDS-PAGE gels (63) or pentameric/hexameric in cross-linking studies (64). The immunoblot analysis showed that the oligomer samples contained SDS-resistant trimers and tetramers as well as unaggregated monomer. Native gels and gel-filtration analysis shows that oligomers are composed of primarily pentamer/hexamer units and some dodecamers (data not shown). Aβ42 dodecamers derived form APP transgenic mice have previously been shown to impair memory when administered into young rats (59). The dimensions derived from our AFM analysis would be consistent with the oligomers forming stable dodecamers. It is likely that the presence of SDS in our immunoblot analysis breaks up larger complexes into more stable SDS-resistant trimers and tetramers.

The solid-state NMR analysis of these oligomers revealed that the same β-strand-turn-β-strand motif observed in fibrils is also found in stable neurotoxic oligomers. Specifically we show that Phe19 packs against Leu34 in the oligomeric state (Figure 2B). It was also shown that unlike the arrangement of fibrils, the β-hairpins are not tightly packed since they do not have a parallel and in-register domain swapped arrangement. This is markedly different form the structural study of neurotoxic oligomers of Aβ40 by Chimon *et al.* (27). According to their measurements, neurotoxic oligomers of Aβ40 are spherical aggregates of 200-400 monomers with diameters of 15-35 nm. Their NMR analysis showed that these large oligomers likely contain parallel β-sheets. Given that Aβ40 does not form stable oligomers, but rather rapidly form extended β-structures, their

data in consistent with Aβ40 oligomers closely resembling the structure of polymerized fibrils. The AFM analysis showed that Aβ42 oligomers are not spherical and have widths of 10-15nm and heights of 2-4nm. We had previously shown that widths of the Aβ42 oligomers are appreciably greater than the heights, and importantly, the heights can be capped by the addition of peptide inhibitors (75). The ability to cap the height of the oligomers, without changing their diameter, supports the data that Aβ42 oligomers are disc-shaped, rather than having a spherical geometry. These stable oligomeric Aβ42 complexes were found to be highly toxic to primary mouse neuronal cultures. The subtle transition to elongated protofibrils resulted in a significant decrease in toxicity. It is thus proposed that the transition from a stable nucleus of β-hairpin units to parallel and in-register, domain-swapped β-sheets results in diminished neuronal toxicity (Figure 3.13).

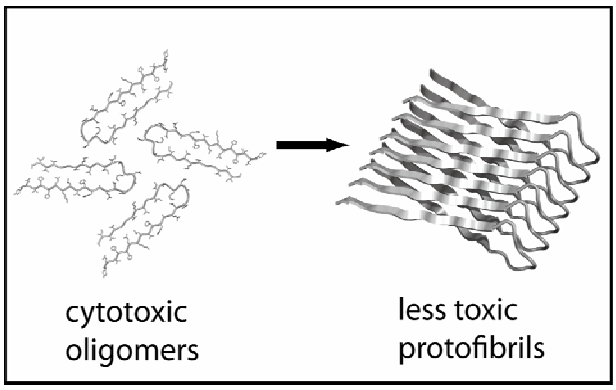

Figure 3.13: Structural transition from stable neurotoxic oligomers to less toxic protofibrils.

Table 3.3: ^{13}C NMR chemical shifts (ppm relative to neat tetramethylsilane) of Aβ42 fibrils and oligomers. Major conformations are shown in bold followed by the relative ratios in parentheses.

	Aβ42 oligomers	Aβ42 fibrils	Aβ40 fibrils (66)
His13/14			
Cε1	136.0	136.1	135.9
Gln15			
Cδ	176.4	176.0	175.5
Phe19			
Cγ	137.1	137.1	**137.1**, 136.1
Cδ1,Cδ2,Cε1,Cε2,Cζ	129.1	128.7	**128.9**, 126.2
Ile31			
CO	174.9, **170.9**, (0.5:1)	**177.2**, 170.1 (1:0.4)	172.3, 172.3
Cα	**60.4**, 55.0 (1:0.5)	**61.2**, 53.4 (1:0.4)	**59.4**, 58.6
Cβ	36.1	41.4, **38.0** (0.3:1)	39.5, **38.2**
Cγ1	26.0	25.8	**25.9**, 24.8
Cγ2	15.5	14.4	19.1, **15.6**
Cδ	12.0	12.5	14.0, **11.1**
Gly33			
CO	168.9	169.2	171.3, **170.0**
Cβ		44.0	47.5, **47.3**
Leu34			
CO	**174.6**, 166.5 (1:0.1)	**173.7**, 167.3 (1:0.1)	171.8, 171.8
Cα	58.0, **50.0** (0.1:1)	57.4, **50.2** (0.1:1)	**53.4**, 52.3
Cβ	44.3	42.6	44.3, **43.9**
Cγ,Cδ1,Cδ2	24.4	24.9	**26.9**, 24.2
Met35			
Cε	15.4	17.2, 15.3 (1:1)	16.0
Gly37			
Cβ	43.3	42.9	43.6, **43.1**
Gly38			
Cβ	43.6	46.7, **41.8** (0.3:1)	43.0
Val39			
CO	173.4	176.8, **170.5** (0.7:1)	172.0
Cα	58.2	**60.7**, 53.7 (1:0.4)	59.3
Cβ	33.8	34.1	33.5
Cγ1,Cγ2	19.0	18.9	19.5
Ala42			
Cβ	19.7	19.9	---

3.10 Conclusion

The structural insights gained from our high-resolution analysis of Aβ42 fibrils and oligomers may lay the groundwork for developing effective therapeutic and diagnostic agents for Alzheimer's disease and other amyloid pathologies. At present, there are no FDA approved pharmaceutical agents that block assembly of neurotoxic Aβ assemblies. This effort has been limited by the lack of structural data on the toxic intermediates involved in Aβ assembly and pathology. Further work on the molecular architecture of forming stable neurotoxic assemblies and the mechanisms by which these oligomers cause neuronal loss are paramount to advancing these efforts.

Chapter 4

Inhibition of Aβ assemblies with designed peptide inhibitors

4.1 Introduction

It has been noted in this study that in fibrillogenic peptides derived from transmembrane helices, glycine often occurs in a GxxxG motif contained within a sequence of hydrophobic amino acids (26). The GxxxG motif places two glycines on the same side of a transmembrane helix or on the same face of a β-sheet. When the individual β-strands within a β-sheet have a parallel orientation and the amino acids are in-register with one another, glycines can form molecular notches or grooves in the surface of the β-sheet that can run the length of the amyloid fibril. The association of β-strands in a parallel and in-register orientation has been observed in several amyloid fibrils (52, 76, 77). In these fibrils, amino acids with large side chains form complementary molecular ridges that can pack into the glycine grooves and stabilize sheet-to-sheet packing (26). This ridge-to-groove packing is the same concept found in the growing body of literature of amyloid-forming sequences forming tight packing "steric zippers" that involve the complementary packing of side-chain residues perpendicular to the long fibril axis (13).

These grooves formed by glycine along the length of fibrils containing GxxxG or GxxxG-like motifs provide a new target for developing therapeutic inhibitors.

The GxxxG motif, itself, may not be critical for stabilizing sheet-to-sheet packing in amyloid fibrils. The occurrence of glycine alone or in other motifs within β-sheets is sufficient to create the corrugated surface if the individual β-strands have a parallel, in-register orientation. For example, α-synuclein, the protein associated with Parkinson's disease, also forms fibrils. It has α-helical secondary structure that converts to β-sheet upon fibril formation (78). The highly fibrillogenic core (residues 60-85) contains several glycines in the context of a long stretch of hydrophobic, mostly β-branched, amino acids similar to the C-terminus of Aβ42 (Figure 1). Importantly, the amino acids in this sequence have been shown to have a parallel, in-register orientation (52). While the GxxxG motif does not occur in the fibrillogenic core of α-synuclein, the core does contain an AxxxG sequence which would result in a similar molecular surface.

The objective of this study was to design peptide inhibitors with alternating small and bulky residues on one face of a β-strand complementary to the GxMxG sequence in the C-terminus of Aβ42. Polar and charged residues on the opposite face were chosen for solubility. A short peptide with the sequence GxFxGxF was previously shown to be effective in preventing fibril formation of a transmembrane fragment of glycophorin A, which contains a well-characterized GxxxG motif (26). The inhibitor peptide placed alternating glycine and phenylalanine on one face of a β-strand. The bulky phenylalanine side chains of the inhibitor were predicted to pack against the glycines in the GxxxG motif of the glycophorin A fibril. In the current work, several variation of the GxFxGxF peptide inhibitors were designed and tested for their ability to block Aβ fibril formation.

The most potent inhibitors would then be used to study the possibilities of de-polymerizing pre-formed fibrils, block oligomer assembly, and inhibit neurotoxicity.

Several peptides were generated (see Table 4.1) and tested for their ability to block amyloid formation of Aβ(1-40). Aβ40 was chosen to initially screen the best peptide inhibitors before moving on to the more toxic Aβ42 peptide.

Table 4.1: Designed peptide inhibitors with alternating GxFxGxF framework.

Inhibitors	**Sequence**
I1	NH_3^+-RGTFEGKF-$CONH_2$
I3	NH_3^+-RGTLEGKL-NH_2
I4	NH_3^+-RGTIEGKI-NH_2
I5	NH_3^+-RGTMEGKM-NH_2
I6	NH_3^+-RATFEAKF-NH_2
I7	NH_3^+-RLTFELKF-$CONH_2$
I8	NH_3^+-RGTFE-$CONH_2$
I9	NH_3^+-RGTFEGK-$CONH_2$
I10	NH_3^+-RGTWEGKW-$CONH_2$
I11	NH_3^+-RGTYEGKY-$CONH_2$
I12	NH_3^+-RSTFESKF-$CONH_2$
I13	NH_3^+-RFTGEFKG-$CONH_2$
I14	NH_3^+-RFTGEF-$CONH_2$

Initial screening was based on Thioflavin T fluorescence assays to determine which inhibitors produced the greatest inhibition of fibrils formation. The results indicated that peptides inhibitors I1 and I10, when applied at a five-fold molar excess, had the most significant effect on inhibiting fibril formation. The effect of these two peptide inhibitors were visualized using transmission EM (see Figure 4.2).

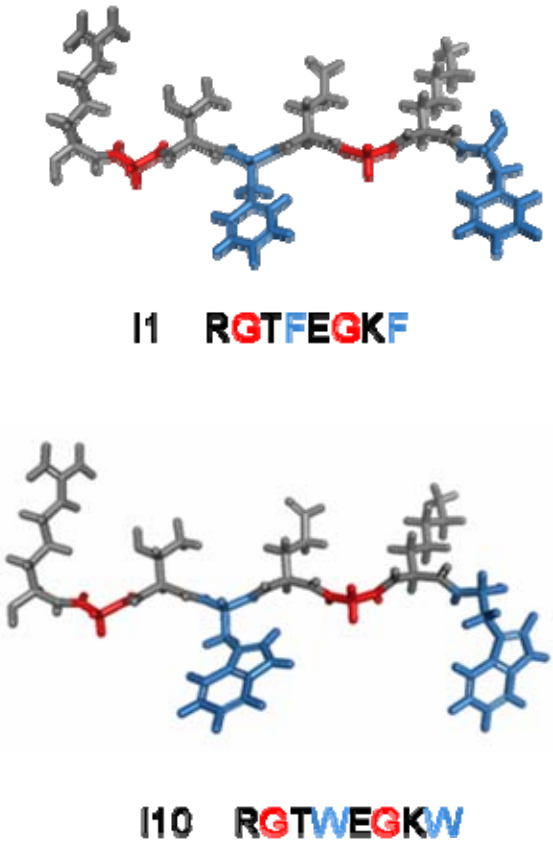

Figure 4.1: Extended structures of peptide inhibitors I1 and I10

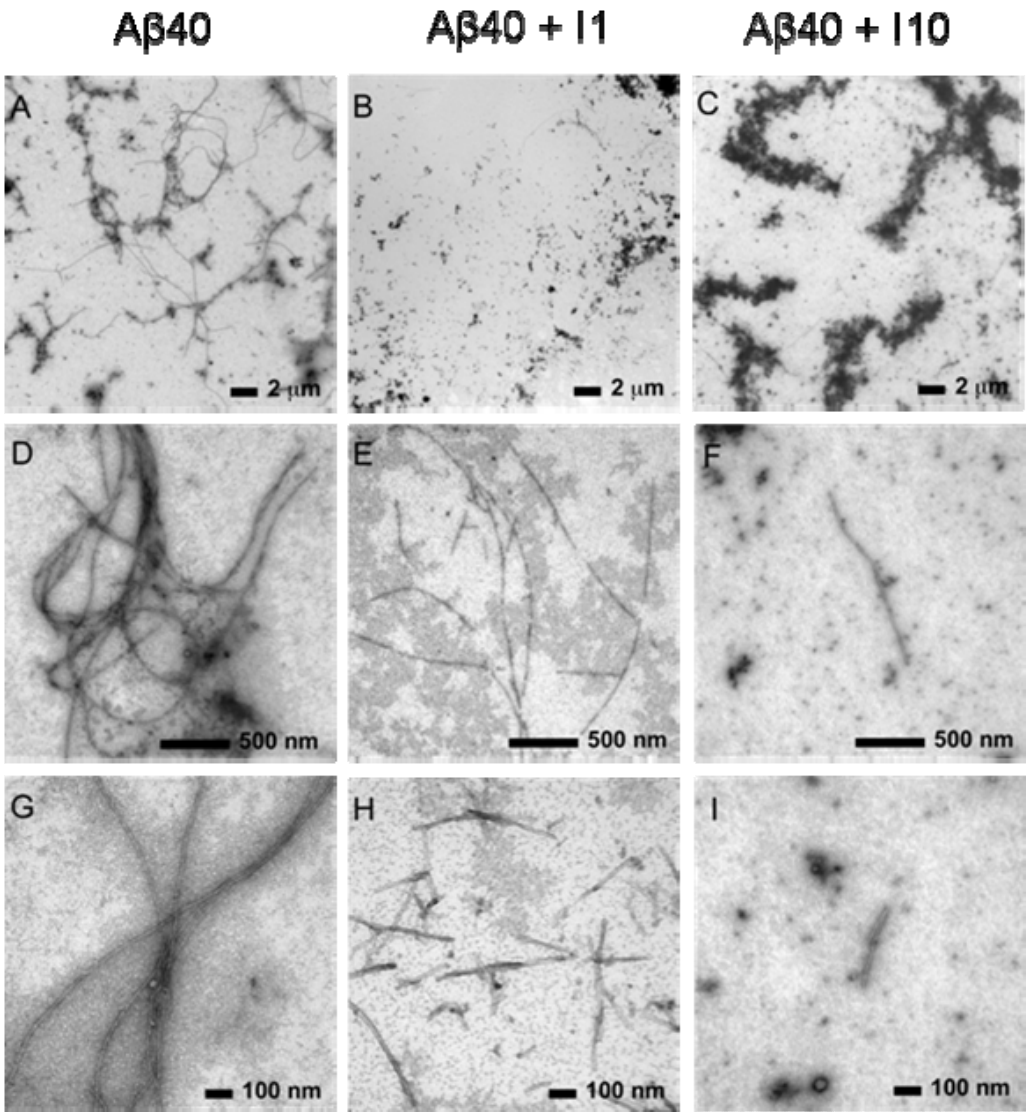

Figure 4.2: EM images of Aβ40 at 3 days with and without added inhibitors. EM of Aβ40 fibrils with and without peptide inhibitors I1 and I10. Images were obtained at three different magnifications: 4800× (A, B, and C), 49 000× (D, E, and F) and 98 000× (G, H, and I). The images were obtained after 72 h of incubation at 37 °C. The concentration of Aβ40 was 40 μM for all experiments, and the molar ratio of Aβ40/inhibitor was 1:1.

EM images are shown at three different magnifications to provide a fair representation of the effect of I1 and I10 on fibril formation. The images obtained at low magnification (upper row) encompass nearly the entire EM grid and are typical of other time points taken in the incubation of Aβ40. Images of Aβ40 in the absence of inhibitor show that Aβ40 forms fibrils with lengths of over 15 mm.

With co-incubation of the designed peptide inhibitors I1 and I10 in a 1:1 molar ratio of Aβ40-to-inhibitor, fewer Aβ40 fibrils are observed at low resolution (Figures 4.2B and C). Large amorphous aggregates are seen instead, particularly in the case of co-incubation with I10 (Figure 4.2C). At higher resolution, one can select regions of the EM fields that contain fibrils. In the case of co-incubation with I1 (Figures 4.2E and H) or I10 (Figures 4.2F and I), we observe shorter fibrils with average lengths between 50 nm and <1 mm. Particularly with I10, fibrils are difficult to detect anywhere on the EM grid.

4.2 Depolymerization of Mature Fibrils by Designed Inhibitors.

The ability of designed peptide inhibitors to depolymerize pre-formed Aβ40 fibrils was investigated. Figure 4.3 shows ThT fluorescence measurements and EM images of Aβ40 fibrils that were allowed to form for 9 days and then split into two parallel samples, one sample without inhibitor and one to which I10 was added at a 1:5 molar ratio of Aβ40-to-inhibitor. Both samples were then incubated at 37°C for 9 additional days. Comparison of the ThT fluorescence shows a decrease of ~25% in the sample with inhibitor during the additional 9 days of incubation consistent with depolymerization of the pre-formed fibrils (Figure 4.3A). EM images of the Aβ40 samples without and with inhibitor are shown in Figures 4.3B and C, respectively. In Figure 4.3B, the sample without inhibitor reveals dense fibrillary tangles after a total of four weeks of incubation. Figure 4.3C

corresponds to a sample of Aβ40 that was allowed to fibrillize for two weeks, and then incubated with I10 for an additional two weeks. Although areas of dense fibrillary tangles and aggregates are observed, distinct areas of clearing with short fragments can readily be identified. Similar experiments using I1 on mature Aβ42 fibrils yielded comparable results (a 40% decrease in ThT fluorescence compared to Aβ without inhibitor and fewer fibrils/more aggregates by EM).

The observation that I10 is able to depolymerize mature Aβ40 fibrils supports the view that these are dynamic structures, and suggests that targeting β-sheet packing may be an effective strategy for depolymerizing amyloid plaques.

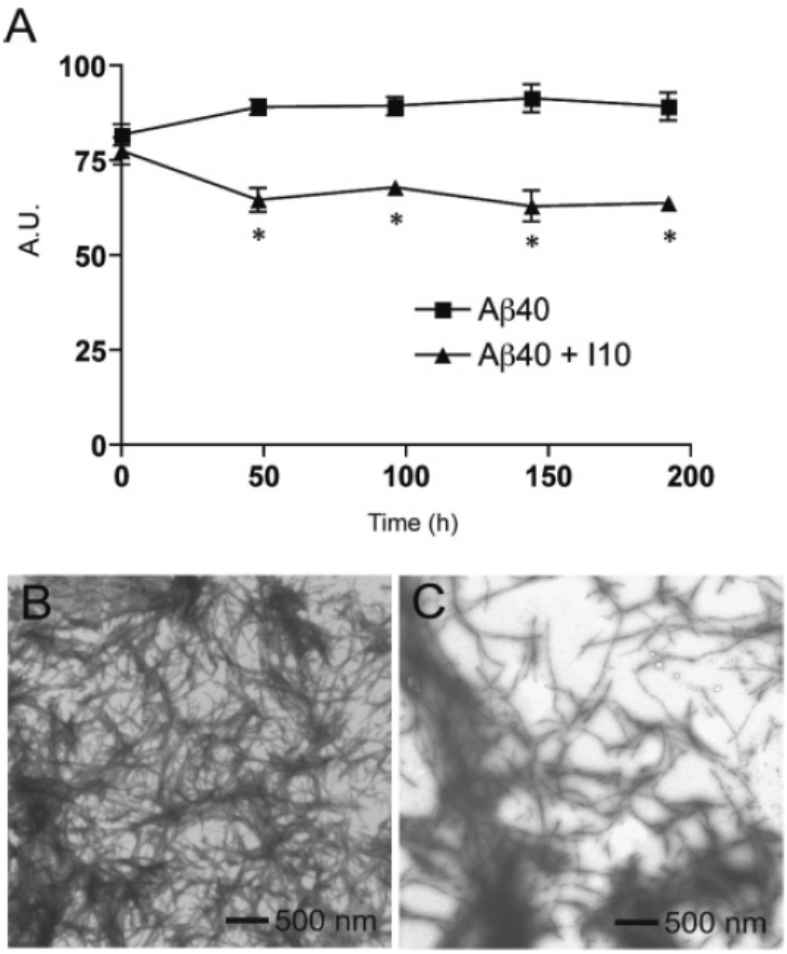

Figure 4.3: Depolymerization of Aβ40 fibrils (A) ThT measurements of Aβ40 with and without inhibitor I10. Day 0 corresponds to the 9 day time point when the sample was split and inhibitor I10 was added to half of the sample. The results represent the mean ± sem for three samples. (B) EM image of Aβ40 fibrils incubated for four weeks without peptide inhibitors. (C) EM image of Aβ40 incubated without peptide inhibitors for two weeks, followed by incubation with the I10 inhibitor for an additional two weeks.

4.3 Inhibition of oligomer assembly with designed peptide inhibitors

The ability of designed inhibitor I1 to affect the structure of the Aβ42 soluble oligomers, the more pathologically significant Aβ isoform, was investigated. Figure 4.4 presents AFM images of Aβ42 oligomers obtained in parallel experiments. Figure 4.4(a) shows Aβ42 oligomers in the absence of inhibitor. With the co-incubation of inhibitor I1 in a 1:20 molar ratio of Aβ to inhibitor (Figure 4.4(b)), oligomer heights are reduced to less than ~4 nm. The reduced sizes of the oligomers in the presence of inhibitor lead to more particles being observed in a given field. Figure 4.4(c) presents a histogram of measured heights of 150 particles (75 particles each with and without I1 inhibitor) observed in field sizes ranging from 150 – 300 nm. Heights are compared since this is the most accurate dimension in AFM measurements. In the absence of inhibitor, Aβ oligomers have a wide distribution of particle heights with a 4.4 nm average height (s.d. 1.4 nm). In contrast, the measured heights of the Aβ oligomers in the presence of inhibitor I1 form a narrow Gaussian distribution with a 2.8 nm average height (s.d. 0.5 nm).

In examining the oligomers in the presence of inhibitor I1, the expected number of particles with measured heights beyond 4.3 nm (3 standard deviations above the mean) is 0.1, and is consistent with the observation of no particles. In the absence of inhibitor, however, over half of the oligomers have heights > 4.3 nm. This indicates that inhibitor I1 has a highly significant effect of reducing the stacking of Aβ42 oligomers. Thus in the presence of I1, packing of Aβ is capped at ~4 nm. In addition, the observation of large numbers of very flat Aβ42 particles with inhibitor supports the conclusion that the

soluble oligomers are disc-shaped structures that result from the stacking of Aβ42 monomers.

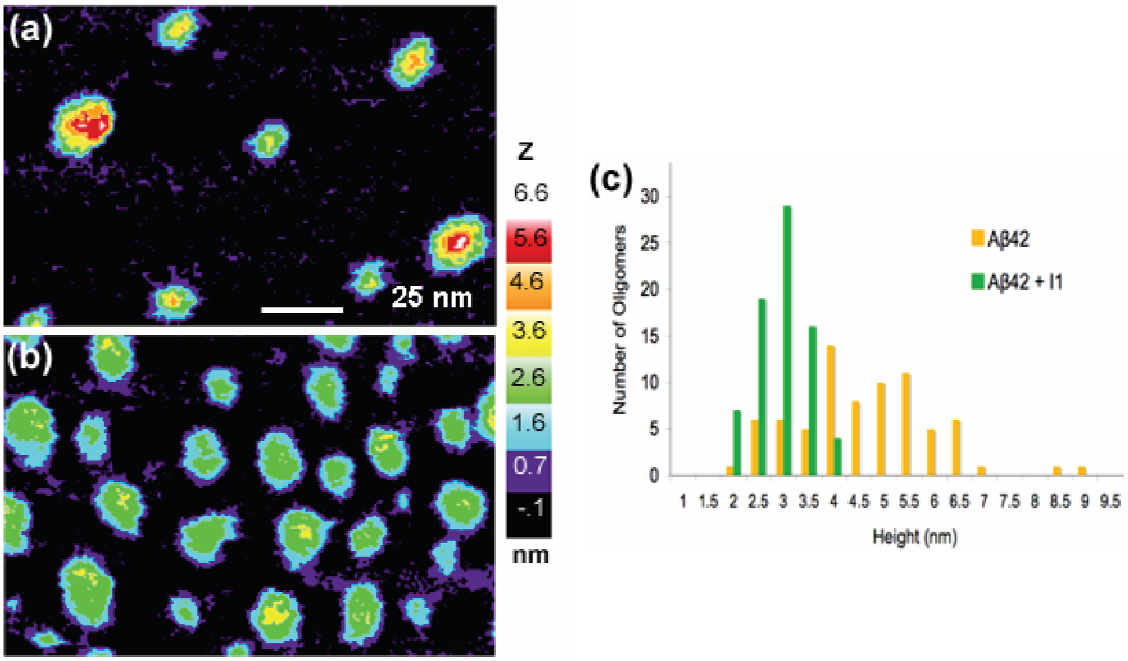

Figure 4.4: High-resolution AFM of high MW oligomers of Aβ42 with designed inhibitors. (a) AFM field without inhibitors, (b) AFM field of Aβ42 with the I1 inhibitor at a molar ratio of 1:20. Samples were adsorbed on mica for 20 min and viewed without washing after fluid was replenished. (c) Histogram of heights of soluble Aβ42 oligomers in the absence of inhibitor (orange) and in the presence of inhibitor I1 (green). The average height was 2.8 nm (s.d. 0.5 nm) in the presence of inhibitor, and 4.4 nm (s.d. 1.4 nm) in the absence of inhibitor.

4.4 Inhibition of neuronal cell toxicity with designed peptide inhibitors

With peptide I10 showing stronger inhibition based on EM images and the ability to depolymerize preformed fibrils, a second generation inhibitor, I21, was developed (see Table 4.2). I21 differs from I10 by replacing the glycine residues with serine and leaving the c-terminus with a free -COOH group. This was an effort to make the peptide inhibitor more hydrophilic. Cell toxicity assays were done using primary mouse cortical neurons. Cells were treated with 2μM Aβ42 pepitdes that had been pre-incubated for 6 h at 37°C in the absence or presence of five-fold excess I1, I10, and I21. Cells were treated for 48 h and then assays for mitochondrial activity using the standard MTT assay (see Methods).

Table 4.2 Sequence of next generation peptide inhibitor I21, compare to I1 and I10

Inhibitors	**Sequence**
I1	NH_3^+-RGTFEGKF-$CONH_2$
I10	NH_3^+-RGTWEGKW-$CONH_2$
I21	NH_3^+-RSTWESKWR-COOH

Figure 4.5 shows the results of the cell toxicity assays. Peptide I21 had a much greater affect of reducing cell toxicity than I1 or I10. The I21 sequence may provide a framework for developing even more potent amyloid-blocking agents.

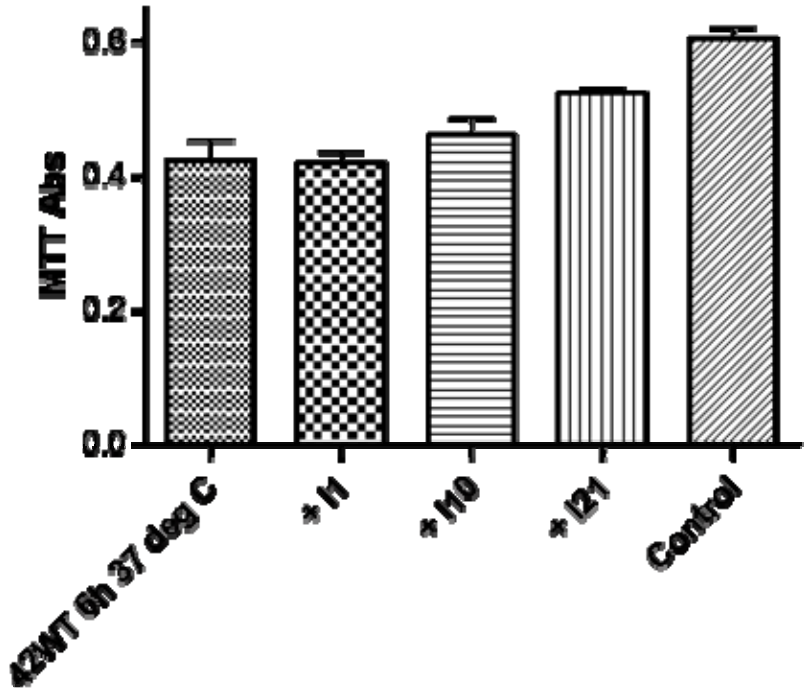

Figure 4.5: Primary mouse cortical neurons treated with Aβ42 in the absence or presence of peptide inhibitors I1, I10, and I21.

4.4 Conclusions

The rationale design of peptide inhibitors to bind to the molecular grooves along the surfaces of β-sheet rich fibrils presents a new modality in approaching amyloid inhibiton. Previous efforts relied on mimicking native sequences or attempting to block the hydrogen bonding direction of fibril growth. It was shown here that peptides with an alternating GxFxGxF can dock into the molecular grooves formed by amyloid fibrils containing a GxMxG motif. This may also represent a general mechanistic approach to blocking the specific side-chain packing arrangements in other amyloid assemblies. Since the core hydrophobic core structures remain very similar for a number of amyloid-forming proteins, a more specific approach such as sequence specific side-chain packing may provide the specificity to target strain-specific pathological phenotypes.

Chapter 5

Structure and inhibition of amyloid fibrils formed from PrP(118-135)

5.1 Introduction

The conversion of cellular prion protein (PrP^{C}) to an altered self-propagating, aggregation prone conformation (PrP^{Sc}) results in a number of prion diseases which are pathologically classified as transmissible spongiform encephalopathies (TSEs) (15). By definition, a prion is a proteinaceuos infectious particle that lacks nucleic acid. The most notable prion diseases include kuru, Gerstmaan-Sträussler-Scheinker Syndrome (GSS), Fatal familial Insomnia (FFI), Creutzfeldt-Jackob disease (CJD) in humans, scrapie in sheep, and bovine spongiform encephalopathy (BSE), often referred to as "mad cow disease." Prion diseases can have infectious, genetic, or sporadic origins and are characterized by widespread neurodegeneration causing rapid progressive dementia, and at present are incurable and fatal (79, 80).

The prion hypothesis that the infectious agent in TSEs was actually a self-replicating protein was based on observations by Griffiths and co-workers that the scrapie

causing agent was insensitive to radiation and other procedures used to inactivate nucleic acids, but was sensitive to treatments that hydrolyze or denature proteins (15). Based on these earlier speculations, Prusiner and co-workers purified the infectious agent form the brains of scrapie-infected hamsters and isolated rod shaped particles containing a protein they termed PrP 27-30, the protease-resistant fragment of the 33 to 35 kDa precursor called PrP^{Sc} (protease resistant protein from scrapie) (81). The cellular gene was later identified and found to correlate with a protein of unknown function (82). Analysis showed that PrP^{C} and PrP^{Sc} had no differences in primary sequence or covalent modifications (83), but were different in their biochemical properties. PrP^{C} is a non-infectious and soluble cellular protein which is sensitive to protease degradation, whereas PrP^{Sc} is an infectious disease-causing protein that forms a protease-resistant core and forms insoluble aggregates (84). Biophysical analysis shows that PrP^{Sc} has an increase in β-sheet content, with PrPC having 43% a—helix and 3% β-sheet and PrP^{Sc} having 30% α-helix and 43% β-sheet (85, 86). The prevailing hypothesis is that infections prions are composed of PrP^{Sc} which self-propagate by catalyzing the conversion of PrP^{C} into the PrP^{Sc} isoform (87). What is a matter of much debate is whether prion disease pathology is caused by the gain of toxic function by PrP^{Sc} or its possible intermediates, or the loss of the cellular function of PrP^{C}. To this end, an enormous amount of effort has been placed the structure and function of both PrP^{C} and PrP^{Sc} (see Figure 5.1).

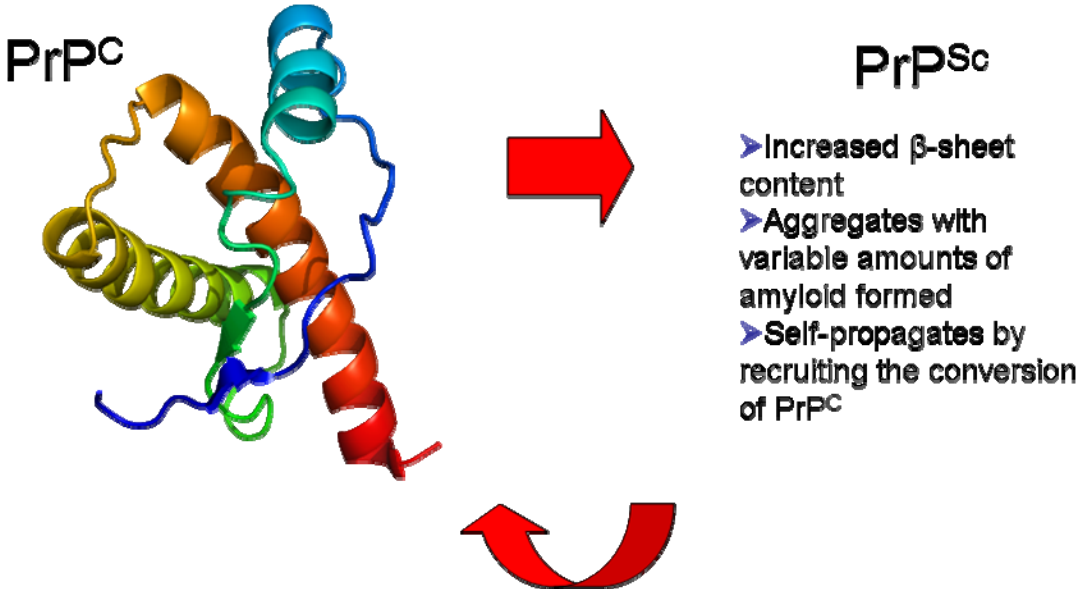

Figure 5.1: Crystal structure (pdb 1d10) of Syrian hamster PrP^{C}(90-231) and the key structural features of PrP^{Sc}

PrP^{C} is highly conserved among many species and expressed on a broad range of tissues including skeletal muscle, kidney, heart, lymph, and the central nervous system (88). PrP^{C} is predominantly localized on the cell surface as an N-glycosylated GPI-anchored protein of ~ 208-209 amino acids (after cleavage of the 22-residue signal peptide). Three dimensional structures of recombinant PrP^{C} in solution have been solved by NMR (see Figure 5.1)(89). The data has shown that residues 23-124 forms a flexible random-coil conformation that contains five octapeptide repeats of PHGGGWSQ (in humans). These repeats have been shown to bind copper, but their function remain

elusive (90). The remainder of the protein forms a globular domain having three α-helices at residues 144-154, 173-194, and 200-228, an anti-parallel β-pleated sheet at residues 128-131 and 161-164, and one disulphide bond between cysteine residues 179 and 214. While these NMR structures provide a useful template to study the properties of PrP^{C} and how these properties may evolve into PrPSc, they are based on recombinant PrP in an aqueous environment that does not account for membrane interactions.

PrPC can be expressed in a number of topological forms. The major product (secPrP) is fully translocated to the outer leaflet of the plasma membrane and bound by its GPI anchor. There are, in addition, two transmembrane forms, one termed C-*trans* transmembrane (^{Ctm}PrP) which has it carboxy-terminus in the ER lumen and the other termed N-*trans* transmembrane (^{Ntm}PrP) which has it amino-terminus in the ER lumen (see Figure 5.2). Normal expression of PrP results in two-thirds secPrP, less than 10% ^{Ctm}PrP, and the rest as ^{Ntm}PrP. Both transmembrane forms span the membrane at the hydrophobic stretch of residues 110-135. The A117V mutation in this region is associated with heritable forms of prion disease including GSS. Other mutations in this region, both naturally occurring and artificial, can lead to increased production of ^{Ctm}PrP, which has been shown to increase neurodegeneration in transgenic mice. Transgenic mice with ^{Ctm}PrP favoring mutations develop scrapie-like neurological symptoms, even without the presence of PrP^{Sc}. Alternatively, healthy mice infected with PrP^{Sc} led to increased production of ^{Ctm}PrP (91, 92). This has led to the hypothesis that the ^{Ctm}PrP may be a key intermediate in prion disease pathology.

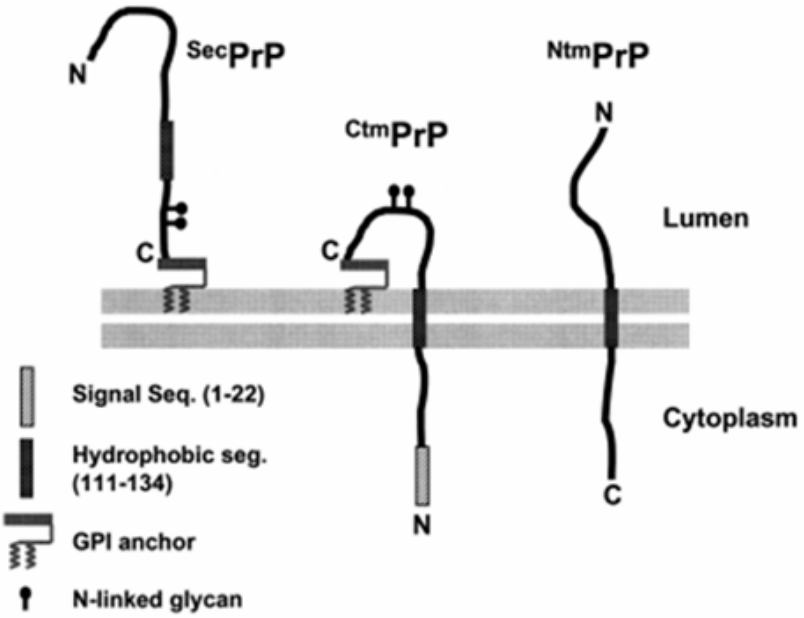

Figure 5.2: Three distinct membrane topologies of PrP ^{C}, from *Chiesa et al.* (84).

The physiological role of PrP remains unclear, although there have been reports that it plays a role in regulating immune responses, signal transduction, copper binding, and synaptic transmission(88). Recent reports have also suggested that PrP^{C} plays a role in the self-renewal of haematopoietic stem cells (93), regulates neurogenesis, and regulates β-secretase cleavage of amyloid precursor protein (APP) (16). The regulation of APP cleavage is of particular interest since this is the first step in the production of toxic Aβ peptides, putatively the major pathological agent is Alzheimer's disease (AD). In the study, overexpression of PrP^{C} in mouse models was found to negatively regulate β-secretase cleavage of APP leading to decreased production of Aβ peptides. Familial prion disease mutants, including the A116V mutation (A117V in humans), were found to lose this negative regulatory affect on APP cleavage. In addition to this link, Alzheimer's

disease and the prion disease CJD share several neuropathological features (94, 95), and polymorphism of Val/Met at position 129 of PrP^{C} is a known risk factor for early onset AD (24 , 25).

Given the physiological significance of residues contained within the hydrophobic transmembrane domain of PrP(110-134) and the previously noted similarity with Aβ in having GxxxG motifs (see Chapter 1), the hydrophobic domain of PrP may play a key role in the conformational conversion of PrP^{C} to PrP^{Sc}. For the purpose of this investigation, the PrP fragment 118-135 was studied for several reasons. PrP(118-135) contains the three consecutive GxxxG motifs and the critical Met129 residue. It also encompasses the majority of the putative transmembrane domain and has previously been shown to form amyloid fibrils (96) and induce apoptotic cell death in rat cortical neurons (97). The purpose of this study was to investigate the molecular details involved in the amyloid fibril formation of PrP(118-135) as well as to test the inhibitory ability of peptide inhibitors designed to block the side-chain packing motif of amyloid fibrils containing GxxxG and GxxxG-like motifs.

The use of solid-state NMR was utilized to investigate the packing arrangement of PrP(118-135) fibrils using a series of peptides with ^{13}C-labels at Gly127, Met129, and Gly131 (see Table 5.1).

Table 5.1. ^{13}C-labeled peptides of PrP(118-135)

Peptide	Sequence
PrP-GG1	118-AGAVVGGL**G(^{13}Cο)**GYML**G(^{13}Cα)**SAMS-135
PrP-GG2	118-AGAVVGGL**G(^{13}Cα)**GYML**G(^{13}Cο)**SAMS-135
PrP-M	118-AGAVVGGLGGY**M(^{13}Cε)**LGSAMS-135

5.2 Characterization of PrP(118-135) fibrils

Samples of PrP(118-135) were incubated with gentle agitation for 4 d at 37°C under physiological salt condition (PBS, pH 7.4). Fibril morphology was verified by transmission EM (see Figure 5.3A). Fibrils are shorter than ones formed by Aβ, but display typical straight, unbranched morphologies. Co-incubation of PrP(118-135) samples with 10% organic solvent (HFIP) resulted in an altered morphology having the periodic twists commonly found in most amyloid fibrils (see Figure 5.3B). The differences in morphologies may reflect the ability of different hydrophobic environments to cause fibril polymorphisms.

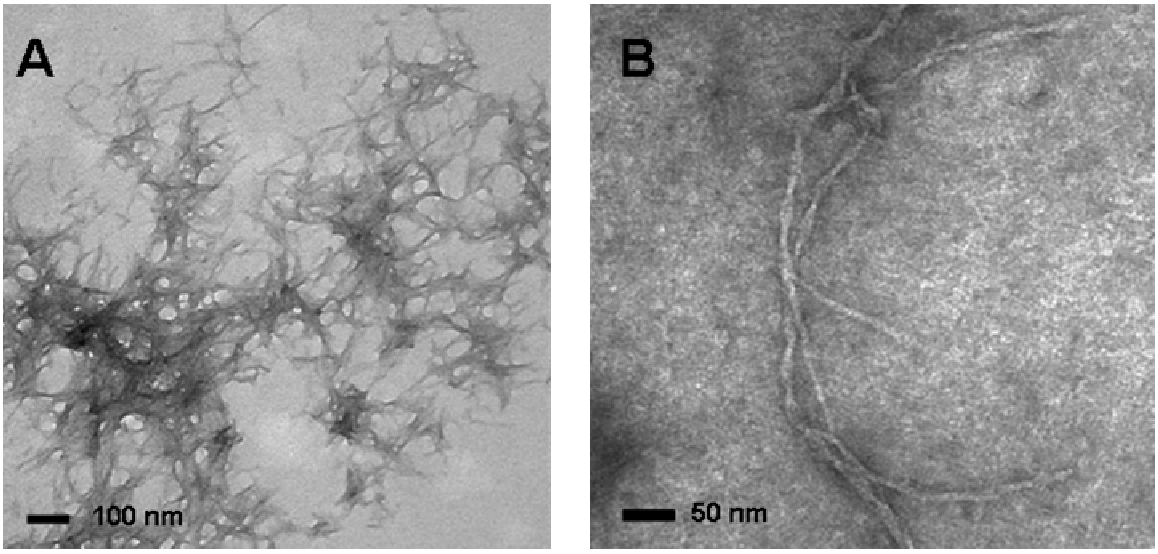

Figure 5.3: TEM of PrP(118-135) fibrils in aqueous conditions (A) and in the presence of 10% HFIP (B).

5.3 Investigation of parallel and in-register orientation of PrP(118-135) fibrils

To investigate whether (PrP118-135) fibrils are composed of β-strands that have polymerized in a parallel and in-register orientation, Gly127 and Gly131 were used as probes to measure inter-strand $^{13}C\ldots{}^{13}C$ dipolar couplings (Figure 5.4). Fibrils samples were prepared containing an equimolar mixture of PrP-GG1:PrP-GG2 (see Table 5.1). Figure 5.4B shows the 2D DARR crosspeak observed between carbonyl carbon (CO) of Gly127 and the Cα of Gly127 on the adjacent β-strand and between the carbonyl carbon

(CO) of Gly131 and the Cα of Gly131 the adjacent β-strand (red boxes). This is indicative of a parallel and in-register orientation of the β-strands in PrP(118-135) fibrils.

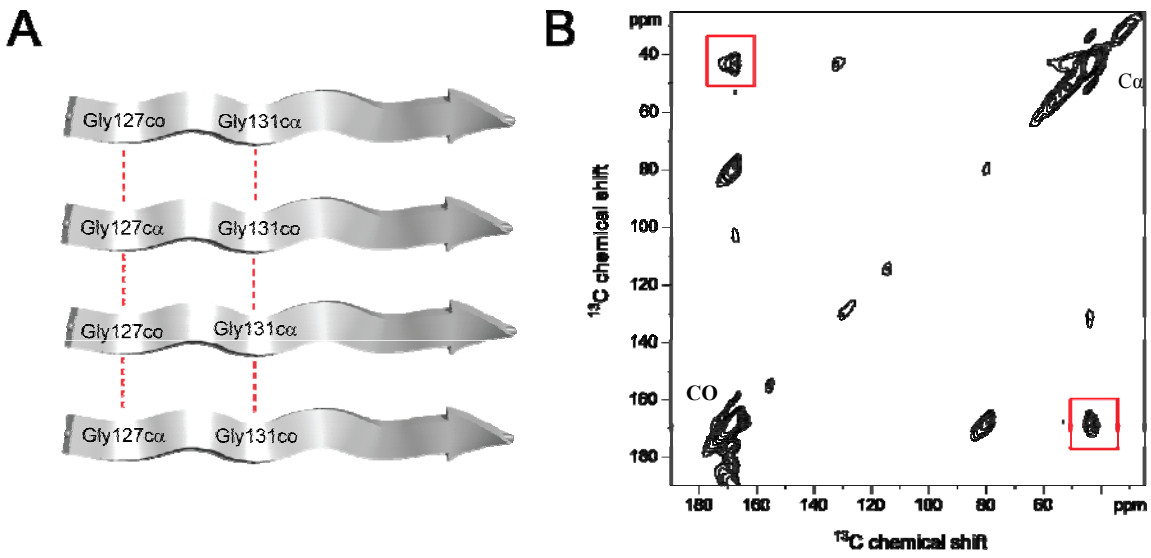

Figure 5.4: Parallel and in-register orientation of amyloid fibrils formed from PrP(118-135). (A) Isotope labeling scheme using an equimolar mixture of PrP-GG1:PrPGG2. (B) 2D DARR spectra showing molecular contacts between ^{13}CO and ^{13}Cα labels of adjacent β-strands along the fibril long axis.

5.4 Investigation of side-chain packing in PrP(118-135) fibrils

The side-chain packing was then investigated in an effort to establish whether Gly127 and Gly129 facilitate the dovetail packing of Met129 in PrP(118-135) fibrils (Figure 5.5). Fibrils were prepared with an equimolar ratio of PrP-GG1:PrP-M peptides (see Table 5.1). The 2D DARR data in Figure 5.5B shows that Met129 makes contact with both Gly127 (blue box) and Gly131 (red box) showing that dovetail packing does occur, but with a polymorphic variability.

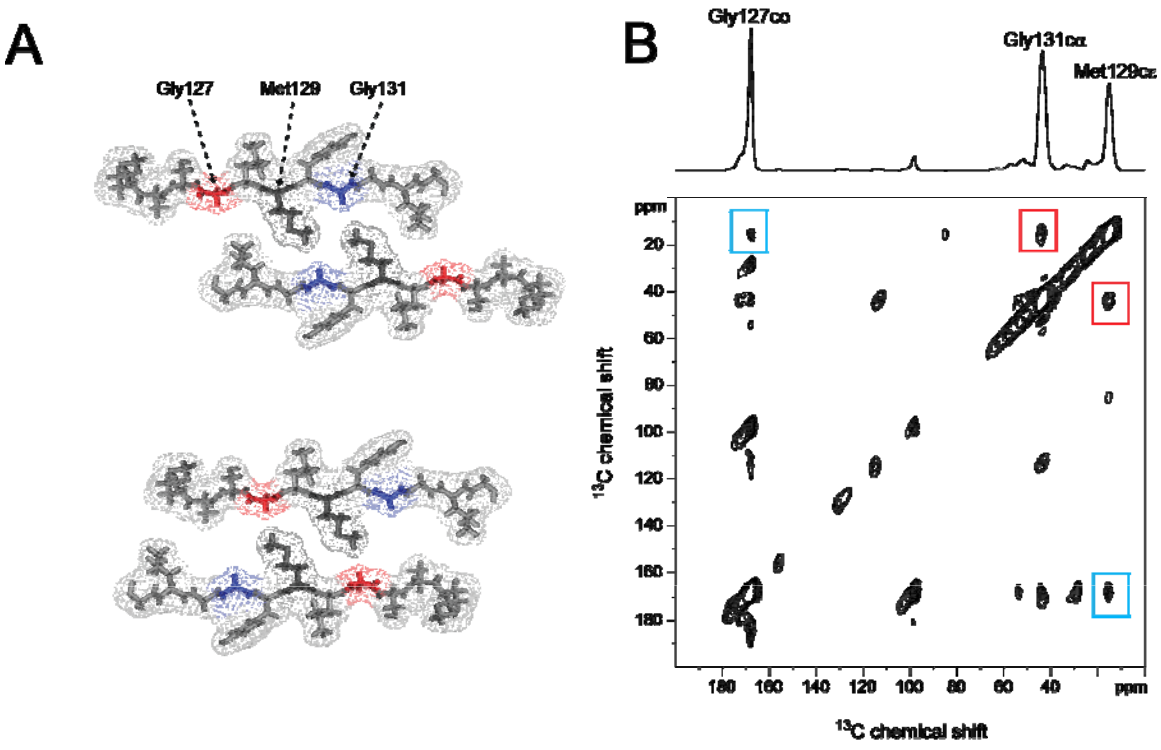

Figure 5.5: PrP(118-135) forms polymorphic steric zipper. (A) Fibrils were formed from an equimolar ratio of PrP-GG1:PrP-M peptides. (B) 2D DARR data showing that Met129-Cε makes molecular contacts with Gly127-CO and Gly131-Cα.

As a control experiment, the same DARR experiment was run using fibrils grown only form the PrP-M peptide. Figure 5.6 shows the one dimensional rows through the Met129-Cε diagonal of DARR spectra of fibrils grown from PrP-GG1:PrP-M peptides (black trace) versus fibrils grown form PrP-M peptides (blue trace). There are no crosspeaks observed in the PrP-M alone sample. This indicates that the Met129 to Gly 127 (~169 ppm) and Gly131 (~42 ppm) are indeed intermolecular side-chain packing interaction.

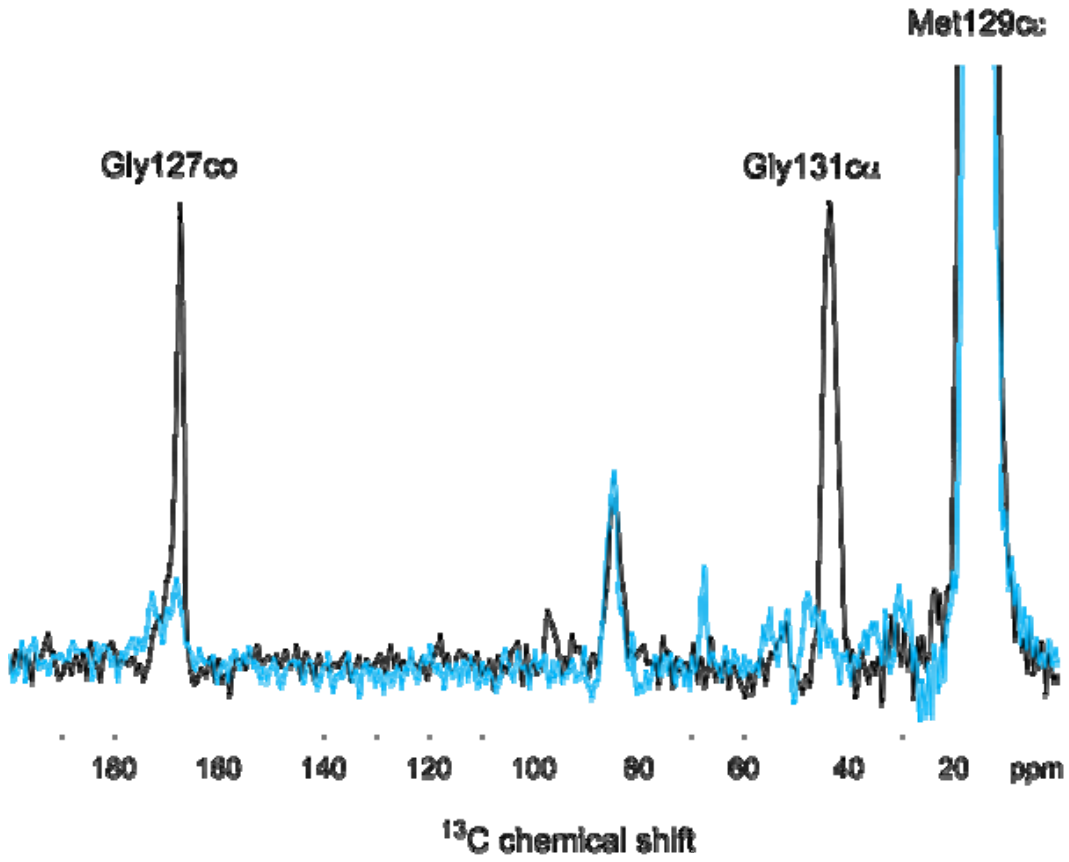

Figure 5.6: Met129 to Gly127/131 contacts are intermolecular. 1D rows through the Met129-Cε chemical shift of DARR experiments of fibrils grown from PrP-GG1:PrP-M peptides (black trace) versus fibrils grown form PrP-M peptides (blue trace).

5.5 Inhibition of PrP(118-135) with designed peptide inhibitors

To investigate whether the designed peptides inhibitors I1 and I10 (see Table 5.2) could block amyloid assembly in PrP(118-135), Thioflavin T fluorescence assays were done to compare the kinetics of fibril formation in the absence or presence of inhibitors. These inhibitors are based on the GxFxGxF motif to complement the GxMxG motifs in the Aβ and in the truncated transmembrane domain of glycophorin A. Figure 5.7 shows the time course of fibril formation of PrP(118-135) in the absence of presence of a five-fold molar excess of inhibitor, as monitored by Thioflavin T binding. The binding of thioflavin T to the cross-β structure of amyloid assemblies shifts its fluorescent properties, allowing for the direct monitoring of amyloid formation at an excitation of 446 nm and emission at 490 nm light. Amyloid formation of PrP(118-135) occurs much faster than that of Aβ, with an undetectable lag phase. The presence of inhibitors I1 and I10 had a modest, but significant effect ($p<0.05$) on inhibiting fibril formation.

Table 5.2: Sequences of designed peptide inhibitors

Peptide Inhibitor	Sequence
I1	NH_3^+-RGTFEGKF-$CONH_2$
I10	NH_3^+-RGTWEGKW-$CONH_2$

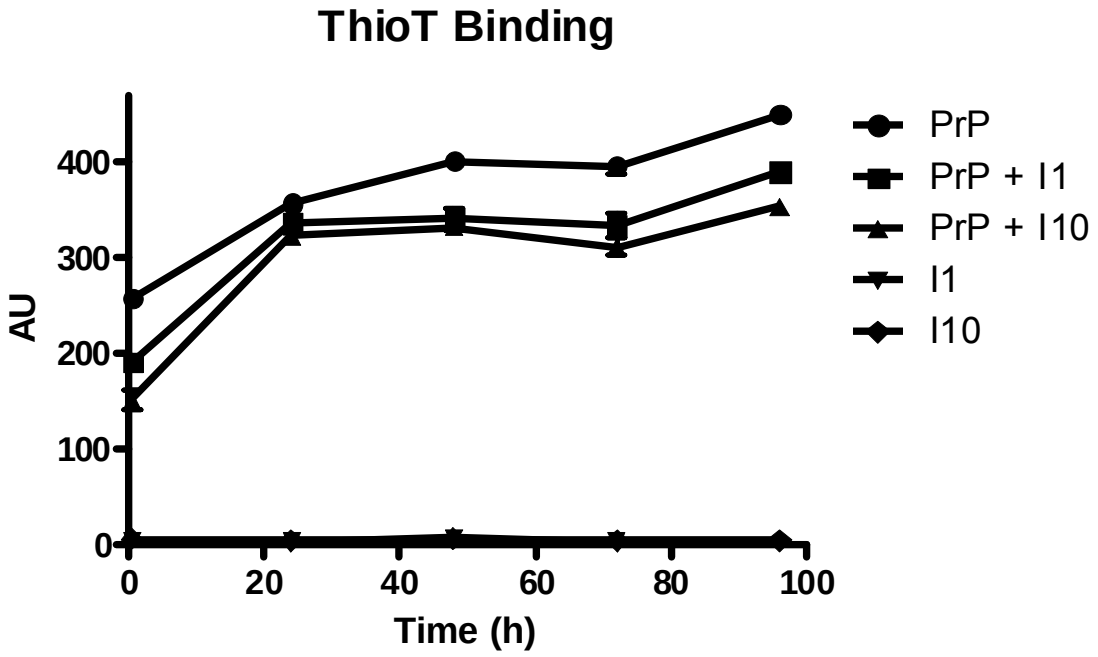

Figure 5.7: Fibril formation of PrP(118-135) in the absence of presence of five-fold molar excess inhibitor.

5.6 Peptide inhibitor I1 blocks Met129 to Gly127/131 packing

The peptide inhibitor I1 was designed to fit into the grooves formed by glycines in a GxMxG motif of parallel and in-register β-sheets. To test whether I1 could dock into the GxMxG motif od PrP(118-135), a DARR experiment was run where PrP(118-135) fibrils were formed using a mixture of PrP-GG1:PrP-M:I1 at 0.5:0.5:1 molar ratios. Higher ratios of inhibitor could not used due to the sample size limitations in solid-state NMR,

which are limited to 100 mg of dry peptide per 4 mm rotor. Figure 5.9 shows the 1D rows through the Met129-Cε chemical shift of DARR experiments of fibrils grown from PrP-GG1:PrP-M peptides (black trace) versus fibrils grown form PrP-GG1:PrP-M:I1 (red trace). A significant decrease is observed in the molecular contacts between Met129 to both Gly127 and Gly131 in the presence of inhibitor I1. This shows that peptide I1 directly influences the side packing of the GxMxG motif in fibrils formed form PrP(118-135).

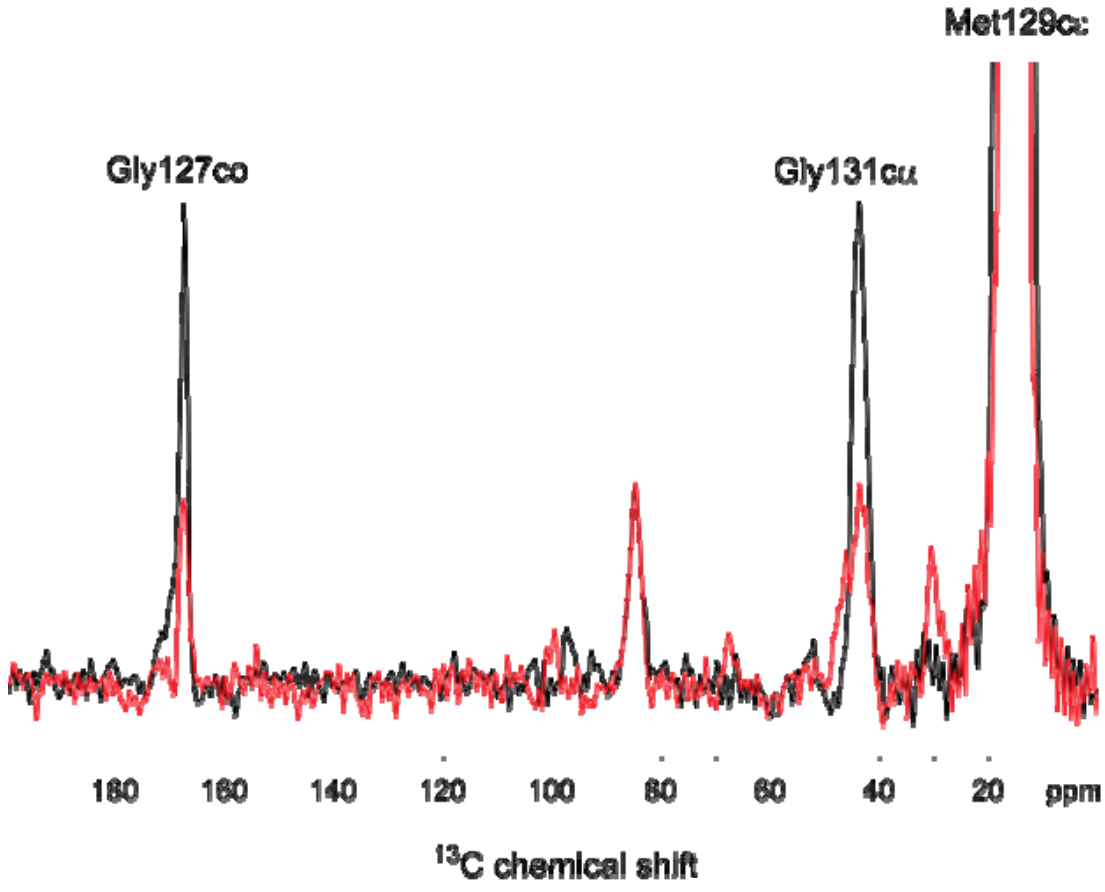

Figure 5.9: Met129 to Gly127/131 packing is reduced in the presence of peptide inhibitor I1. 1D rows through the Met129-Cε chemical shift of DARR experiments of fibrils grown from PrP-GG1:PrP-M peptides (black trace) versus fibrils grown form PrP-GG1:PrP-M:I1 (red trace).

5.7 Conclusion

Amyloid fibrils derived from the transmembrane helices of amyloid precursor protein, glycophorin A, and human prion protein contain glycines in a GxMxG sequence motif. Individual β-strands in amyloid fibrils formed from both glycophorin A and the Aβ peptides have a parallel and in-register orientation. The occurrence of glycine within these fibrils produces molecular grooves that run the length of the fibril, and it has been demonstrated that the association of β-sheets to mature fibrils is mediated by ridges-into-grooves packing involving glycine and methionine. Moreover, this specific packing can be blocked by the use of designed peptide inhibitors that mimic this interaction. Thus, the GxFxGxF inhibitor framework may also work to inhibit other amyloid forming sequences with similar sequence motifs.

Chapter 6

Conclusions

While the initial investigation of this study focused on the role of conserved glycine residues in the stabilization of β-sheet fibrils derived from α -helical transmembrane precursors, several structural and mechanistic insights were discovered along the path. In the detailed molecular investigation of oligomers and fibrils formed from the amyloid-β(1-42) peptide, it was revealed that the specific side-chain packing involved in β-hairpin formation formed early on in the aggregation pathway. The distinct molecular switch to having parallel and in-register domain swapped β-strands leads to a decrease in neurotoxicity. AFM and immunoblot analysis of the β-hairpin units in oligomers revealed that they form relatively stable states at low temperature and salt conditions. The oligomers are relatively monodispersed and are likely made up of dodecamers that contain more-structured SDS-resistant trimer/tetramer bundles. Further investigation into the structural forces involved in holding these oligomers into a toxic conformation is recommended.

When investigating the use of inhibitors to block Aβ toxicity, it was discovered that designing peptides with alternating small and large residues was an effective method to provide surface complementarity to block the native side-chain packing arrangement. Making these inhibitors more soluble also added to their potency. Targeting specific side-chain packing motifs may provide specificity to blocking polymorphic strains observed in several protein misfolding diseases, including the transmissible spongiform encephalopathies.

Lastly, the precise β-strand orientations and side-chain packing architecture was deduced of the fibril forming peptide derived from the putative transmembrane of PrP. Understanding this transition from α-helical structure to β-sheet fibrils may help to unlock the mystery that still surrounds prion diseases. Importantly, the designed peptide inhibitors that blocked fibrils formed from both Aβ and the transmembrane domain of glycophorin A, was found to not only inhibit but disrupt the side-chain packing order of PrP(118-135) fibrils. This adds to the evidence that rationally designing inhibitors to complement surface topology may prove to be a useful therapeutic strategy.

Bibliography

1. Chiti F & Dobson CM (2006) Protein misfolding, functional amyloid, and human disease. *Annu. Rev. Biochem.* 75:333-366.
2. Lashuel HA & Lansbury PT (2006) Are amyloid diseases caused by protein aggregates that mimic bacterial pore-forming toxins? *Q. Rev. Biophys.* 39(2):167-201.
3. Ferreira ST, Vieira MNN, & De Felice FG (2007) Soluble protein oligomers as emerging toxins in Alzheimer's and other amyloid diseases. *IUBMB Life* 59(4-5):332-345.
4. Kodali R & Wetzel R (2007) Polymorphism in the intermediates and products of amyloid assembly. *Curr. Opin. Struct. Biol.* 17(1):48-57.
5. Fändrich M (2007) On the structural definition of amyloid fibrils and other polypeptide aggregates. *Cell. Mol. Life. Sci.* 64(16):2066-2078.
6. Eanes ED & Glenner GG (1968) X-ray diffraction studies on amyloid filaments. *J. Histochem. Cytochem.* 16(11):673-&.
7. Sunde M*, et al.* (1997) Common core structure of amyloid fibrils by synchrotron X-ray diffraction. *J. Mol. Biol.* 273(3):729-739.
8. Spencer RG*, et al.* (1991) An unusual peptide conformation may precipitate amyloid formation in Alzheimer's disease: application of solid-state NMR to the determination of protein secondary structure. *Biochemistry* 30:10382-10387.
9. Lansbury PT, Jr.*, et al.* (1995) Structural model for the β-amyloid fibril based on interstrand alignment of an antiparallel-sheet comprising a C-terminal peptide. *Nat. Struct. Biol.* 2:990-998.
10. Tycko R (2006) Molecular structure of amyloid fibrils: Insights from solid-state NMR. *Q. Rev. Biophys.* 39(1):1-55.
11. Paravastua AK, Leapman RD, Yau WM, & Tycko R (2008) Molecular structural basis for polymorphism in Alzheimer's β-amyloid fibrils. *Proc. Natl. Acad. Sci. U.S.A.* 105(47):18349-18354.
12. Nelson R*, et al.* (2005) Structure of the cross-β spine of amyloid-like fibrils. *Nature* 435(7043):773-778.
13. Nelson R & Eisenberg D (2006) Recent atomic models of amyloid fibril structure. *Curr. Opin. Struct. Biol.* 16(2):260-265.
14. Harper JD & Lansbury PT (1997) Models of amyloid seeding in Alzheimier's disease and scrapie: Mechanistic truths and physiological consequences of the time-dependent solubility of amyloid proteins. *Annu. Rev. Biochem.* 66:385-407.
15. Prusiner SB (1998) Prions. *Proc. Natl. Acad. Sci. U.S.A.* 95(23):13363-13383.
16. Parkin ET*, et al.* (2007) Cellular prion protein regulates β-secretase cleavage of the Alzheimer's amyloid precursor protein. *Proc. Natl. Acad. Sci. U.S.A.* 104(26):11062-11067.

17. Taylor DR & Hooper NM (2007) Role of lipid rafts in the processing of the pathogenic prion and Alzheimer's amyloid-β proteins. *Seminars in Cell & Developmental Biology* 18(5):638-648.
18. Javadpour MM, Eilers M, Groesbeek M, & Smith SO (1999) Helix packing in polytopic membrane proteins: role of glycine in transmembrane helix association. *Biophys. J.* 77:1609-1618.
19. Eilers M, Patel AB, Liu W, & Smith SO (2002) Comparison of helix interactions in membrane and soluble α-bundle proteins. *Biophys. J.* 82(5):2720-2736.
20. Russ WP & Engelman DM (2000) The GxxxG motif: a framework for transmembrane helix-helix association. *J. Mol. Biol.* 296:911-919.
21. Kleiger G, Grothe R, Mallick P, & Eisenberg D (2002) GXXXG and AXXXA: Common α-helical interaction motifs in proteins, particularly in extremophiles. *Biochemistry* 41(19):5990-5997.
22. Kanski J, Varadarajan S, Aksenova M, & Butterfield DA (2002) Role of glycine-33 and methionine-35 in Alzheimer's amyloid β-peptide 1-42-associated oxidative stress and neurotoxicity. *Biochim. Biophys. Acta-Mol. Basis Dis.* 1586(2):190-198.
23. Smith DP*, et al.* (2006) Copper-mediated amyloid-β toxicity is associated with an intermolecular histidine bridge. *J. Biol. Chem.* 281(22):15145-15154.
24. Dermaut B*, et al.* (2003) PRNP Val129 homozygosity increases risk for early-onset Alzheimer's disease. *Ann. Neurol.* 53(3):409-412.
25. Riemenschneider M*, et al.* (2004) Prion protein codon 129 polymorphism and risk of Alzheimer disease. *Neurology* 63(2):364-366.
26. Liu W*, et al.* (2005) Structural role of glycine in amyloid fibrils formed from transmembrane ⟨-helices. *Biochemistry* 44(9):3591-3597.
27. Chimon S*, et al.* (2007) Evidence of fibril-like β-sheet structures in a neurotoxic amyloid intermediate of Alzheimer's β-amyloid. *Nat. Struct. Mol. Biol.* 14(12):1157-1164.
28. Hansma PK*, et al.* (1994) Tapping mode atomic-force microscopy in liquids. *Appl. Phys. Lett.* 64(13):1738-1740.
29. Han WH, Lindsay SM, & Jing TW (1996) A magnetically driven oscillating probe microscope for operation in liquids. *Appl. Phys. Lett.* 69(26):4111-4113.
30. Guthold M*, et al.* (1999) Direct observation of one-dimensional diffusion and transcription by Escherichia coli RNA polymerase. *Biophys. J.* 77(4):2284-2294.
31. Binnig G, Quate CF, & Gerber C (1986) Atomic force microscope. *Phys. Rev. Lett.* 56(9):930-933.
32. Müller DJ*, et al.* (2003) Observing membrane protein diffusion at subnanometer resolution. *J. Mol. Biol.* 327(5):925-930.
33. Hansma HG, Kasuya K, & Oroudjev E (2004) Atomic force microscopy imaging and pulling of nucleic acids. *Curr. Opin. Struct. Biol.* 14(3):380-385.
34. Metz G, Wu X, & Smith SO (1994) Ramped-amplitude cross polarization in magic angle spinning NMR. *J. Magn. Reson. A.* 110:219-227.

35. Bennett AE, Rienstra CM, Auger M, Lakshmi KV, & Griffin RG (1995) Heteronuclear decoupling in rotating solids. *J. Chem. Phys.* 103:6951-6958.
36. Takegoshi K, Nakamura S, & Terao T (2001) ^{13}C-^{1}H dipolar-assisted rotational resonance in magic-angle spinning NMR. *Chem. Phys. Lett.* 344(5-6):631-637.
37. Crocker E*, et al.* (2004) Dipolar assisted rotational resonance NMR of tryptophan and tyrosine in rhodopsin. *J. Biomol. NMR* 29(1):11-20.
38. Levitt MH (2001) *Spin Dynamics* (John Wiley & Sons, Ltd, Chichester) 1 Ed pp 543-546.
39. Cavanagh J, Fairbrother WJ, Palmer AG, & Skelton NJ (1996) *Protein NMR Spectroscopy* (Academic Press, San Diego).
40. Ernst RR, Bodenhausen G, & Wokaun A (1987) *Principles of Nuclear Magnetic Resonance in One and Two Dimensions* (Clarendon Press, Oxford).
41. Selkoe DJ (2003) Folding proteins in fatal ways. *Nature* 426(6968):900-904.
42. Masters CL*, et al.* (1985) Amyloid plaque core protein in Alzheimer disease and Down syndrome. *Proc. Natl. Acad. Sci. U.S.A.* 82(12):4245-4249.
43. Kang J*, et al.* (1987) The precursor of Alzheimer's disease amyloid A4 protein resembles a cell-surface receptor. *Nature* 325(6106):733-736.
44. Jarrett JT, Berger EP, & Lansbury PT (1993) The carboxy terminus of the β-amyloid protein is critical for the seeding of amyloid formation - Implications for the pathogenesis of Alzheimer's disease. *Biochemistry* 32(18):4693-4697.
45. Roher AE*, et al.* (1993) β-amyloid-(1-42) is a major component of cerebrovascular amyloid deposits - Implications for the pathology of Alzheimer-disease. *Proc. Natl. Acad. Sci. U.S.A.* 90(22):10836-10840.
46. Iwatsubo T, Saido TC, Mann DM, Lee VM, & Trojanowski JQ (1996) Full-length amyloid-β (1-42(43)) and amino-terminally modified and truncated amyloid-β 42(43) deposit in diffuse plaques. *Am. J. Pathol.* 149(6):1823-1830.
47. Burdick D*, et al.* (1992) Assembly and aggregation properties of synthetic Alzheimer's A4/β amyloid peptide analogs. *J. Biol. Chem.* 267(1):546-554.
48. Borchelt DR*, et al.* (1996) Familial Alzheimer's disease-linked presenilin 1 variants elevate Abeta1-42/1-40 ratio in vitro and in vivo. *Neuron* 17(5):1005-1013.
49. Mayeux R*, et al.* (1999) Plasma amyloid beta-peptide 1-42 and incipient Alzheimer's disease. *Ann. Neurol.* 46(3):412-416.
50. Thinakaran G & Koo EH (2008) Amyloid precursor protein trafficking, processing, and function. *J. Biol. Chem.* 283(44):29615-29619.
51. Antzutkin ON, Leapman RD, Balbach JJ, & Tycko R (2002) Supramolecular structural constraints on Alzheimer's β -amyloid fibrils from electron microscopy and solid-state nuclear magnetic resonance. *Biochemistry* 41(51):15436-15450.
52. Torok M*, et al.* (2002) Structural and dynamic features of Alzheimer's Aβ peptide in amyloid fibrils studied by site-directed spin labeling. *J. Biol. Chem.* 277(43):40810-40815.
53. Lührs T*, et al.* (2005) 3D structure of Alzheimer's amyloid-β (1-42) fibrils. *Proc. Natl. Acad. Sci. U.S.A.* 102(48):17342-17347.

54. Eckman CB, *et al.* (1997) A new pathogenic mutation in the APP gene (1716V) increases the relative proportion of Aβ42(43). *Hum. Mol. Genet.* 6(12):2087-2089.
55. McLean CA, *et al.* (1999) Soluble pool of Aβ amyloid as a determinant of severity of neurodegeneration in Alzheimer's disease. *Ann. Neurol.* 46(6):860-866.
56. Lue LF, *et al.* (1999) Soluble amyloid β peptide concentration as a predictor of synaptic change in Alzheimer's disease. *Am. J. Pathol.* 155(3):853-862.
57. Hsia AY, *et al.* (1999) Plaque-independent disruption of neural circuits in Alzheimer's disease mouse models. *Proc. Natl. Acad. Sci. U.S.A.* 96(6):3228-3233.
58. Walsh DM, *et al.* (2002) Naturally secreted oligomers of amyloid β protein potently inhibit hippocampal long-term potentiation in vivo. *Nature* 416(6880):535-539.
59. Lesne S, *et al.* (2006) A specific amyloid-β protein assembly in the brain impairs memory. *Nature* 440(7082):352-357.
60. Caughey B & Lansbury PT (2003) Protofibrils, pores, fibrils, and neurodegeneration: Separating the responsible protein aggregates from the innocent bystanders. *Annu. Rev. Neurosci.* 26:267-298.
61. Glabe CG (2006) Common mechanisms of amyloid oligomer pathogenesis in degenerative disease. *Neurobiol. Aging* 27(4):570-575.
62. McGowan E, *et al.* (2005) Aβ42 is essential for parenchymal and vascular amyloid deposition in mice. *Neuron* 47(2):191-199.
63. Chen YR & Glabe CG (2006) Distinct early folding and aggregation properties of Alzheimer amyloid-β peptides Aβ40 and Aβ42 - Stable trimer or tetramer formation by Aβ42. *J. Biol. Chem.* 281(34):24414-24422.
64. Bitan G, Vollers SS, & Teplow DB (2003) Elucidation of primary structure elements controlling early amyloid β-protein oligomerization. *J. Biol. Chem.* 278(37):34882-34889.
65. Masuda Y, *et al.* (2008) Verification of the C-terminal intramolecular β-sheet in Aβ42 aggregates using solid-state NMR: Implications for potent neurotoxicity through the formation of radicals. *Bioorg. Med. Chem. Lett.* 18(11):3206-3210.
66. Petkova AT, Yau WM, & Tycko R (2006) Experimental constraints on quaternary structure in Alzheimer's β-amyloid fibrils. *Biochemistry* 45(2):498-512.
67. Simmons LK, *et al.* (1994) Secondary structure of amyloid β-peptide correlates with neurotoxic activity *in vitro*. *Mol. Pharmacol.* 45(3):373-379.
68. Soto C, Castano EM, Kumar RA, Beavis RC, & Frangione B (1995) Fibrillogenesis of synthetic amyloid-β peptides is dependent on their initial secondary structure. *Neurosci. Lett.* 200(2):105-108.
69. Tamm LK & Tatulian SA (1997) Infrared spectroscopy of proteins and peptides in lipid bilayers. *Q. Rev. Biophys.* 30:365-429.

70. Walsh DM, *et al.* (1999) Amyloid β-protein fibrillogenesis - Structure and biological activity of protofibrillar intermediates. *J. Biol. Chem.* 274(36):25945-25952.
71. Sato T, *et al.* (2006) Inhibitors of amyloid toxicity based on β-sheet packing of Aβ40 and Aβ42. *Biochemistry* 45(17):5503-5516.
72. Johansson AS, *et al.* (2007) Attenuated amyloid-β aggregation and neurotoxicity owing to methionine oxidation. *Neuroreport* 18(6):559-563.
73. Hou LM, Kang I, Marchant RE, & Zagorski MG (2002) Methionine 35 oxidation reduces fibril assembly of the amyloid A®-(1-42) peptide of Alzheimer's disease. *J. Biol. Chem.* 277(43):40173-40176.
74. Bitan G, *et al.* (2003) A molecular switch in amyloid assembly: Met^{35} and amyloid β-protein oligomerization. *J. Am. Chem. Soc.* 125(50):15359-15365.
75. Mastrangelo IA, *et al.* (2006) High-resolution atomic force microscopy of soluble Aβ42 oligomers *J. Mol. Biol.* 358(1):106-119
76. Benzinger TLS, *et al.* (1998) Propagating structure of Alzheimer's β-amyloid(10-35) is parallel β-sheet with residues in exact register. *Proc. Natl. Acad. Sci. U.S.A.* 95(23):13407-13412.
77. Antzutkin ON, *et al.* (2000) Multiple quantum solid-state NMR indicates a parallel, not antiparallel, organization of β-sheets in Alzheimer's β-amyloid fibrils. *Proc. Natl. Acad. Sci. U.S.A.* 97(24):13045-13050.
78. Kessler JC, Rochet JC, & Lansbury PT (2003) The N-terminal repeat domain of α-synuclein inhibits β-sheet and amyloid fibril formation. *Biochemistry* 42(3):672-678.
79. Glatzel M, *et al.* (2003) Human prion diseases: epidemiology and integrated risk assessment. *Lancet Neurol.* 2(12):757-763.
80. Collins SJ, Lawson VA, & Masters CL (2004) Transmissible spongiform encephalopathies. *Lancet* 363(9402):51-61.
81. Prusiner SB, Groth DF, Bolton DC, Kent SB, & Hood LE (1984) Purification and structural studies of a major scrapie prion protein. *Cell* 38(1):127-134.
82. Prusiner S, *et al.* (1985) Molecular-Cloning Studies Demonstrate That Cellular Genomic DNA Encodes the Scrapie Prion Protein. *Clin. Res.* 33(2):A565-A565.
83. Stahl N, *et al.* (1993) Structural studies of the scrapie prion protein using mass-spectrometry and amino-acid sequencing. *Biochemistry* 32(8):1991-2002.
84. Chiesa R & Harris DA (2001) Prion diseases: What is the neurotoxic molecule? *Neurobiol. Dis.* 8(5):743-763.
85. Caughey BW, *et al.* (1991) Secondary structure analysis of the scrapie-associated protein Prp 27-30 in water by infrared spectroscopy. *Biochemistry* 30(31):7672-7680.
86. Pan KM, *et al.* (1993) Conversion of α-helices into β-sheets features in the formation of the scrapie prion proteins. *Proc. Natl. Acad. Sci. U.S.A.* 90(23):10962-10966.
87. Cohen FE & Prusiner SB (1998) Pathologic conformations of prion proteins. *Annu. Rev. Biochem.* 67:793-819.

88. Aguzzi A & Polymenidou M (2004) Mammalian prion biology: One century of evolving concepts. *Cell* 116(2):313-327.
89. Riek R*, et al.* (1996) NMR structure of the mouse prion protein domain PrP(121-321). *Nature* 382(6587):180-182.
90. Jones CE, Klewpatinond M, Abdelraheim SR, Brown DR, & Viles JH (2005) Probing copper^{2+} binding to the prion protein-using diamagnetic nickel^{2+} and ^{1}H NMR: The unstructured N terminus facilitates the coordination of six copper^{2+} ions at physiological concentrations. *J. Mol. Biol.* 346(5):1393-1407.
91. Hegde RS*, et al.* (1998) A transmembrane form of the prion protein in neurodegenerative disease. *Science* 279(5352):827-834.
92. Stewart RS, Piccardo P, Ghetti B, & Harris DA (2005) Neurodegenerative illness in transgenic mice expressing a transmembrane form of the prion protein. *J. Neurosci.* 25(13):3469-3477.
93. Zhang CC, Steele AD, Lindquist S, & Lodish HF (2006) Prion protein is expressed on long-term repopulating hematopoietic stem cells and is important for their self-renewal. *Proc. Natl. Acad. Sci. U.S.A.* 103(7):2184-2189.
94. Hainfellner JA*, et al.* (1998) Coexistence of Alzheimer-type neuropathology in Creutzfeldt-Jakob disease. *Acta Neuropathol.* 96(2):116-122.
95. Voigtländer T*, et al.* (2001) Marked increase of neuronal prion protein immunoreactivity in Alzheimer's disease and human prion diseases. *Acta Neuropathol.* 101(5):417-423.
96. Pillot T*, et al.* (1997) The 118-135 peptide of the human prion protein forms amyloid fibrils and induces liposome fusion. *J. Mol. Biol.* 274(3):381-393.
97. Pillot T*, et al.* (2000) A nonfibrillar form of the fusogenic prion protein fragment [118-135] induces apoptotic cell death in rat cortical neurons. *J. Neurochem.* 75(6):2298-2308.